

ATMOSPHERIC PARAMETERS OF FIELD L AND T DWARFS¹

MICHAEL C. CUSHING², MARK S. MARLEY³, D. SAUMON⁴, BRANDON C. KELLY⁵, WILLIAM D. VACCA⁶, JOHN T. RAYNER⁷,
RICHARD S. FREEDMAN⁸, KATHARINA LODDERS⁹, & THOMAS L. ROELLIG¹⁰

Accepted for publication in ApJ

ABSTRACT

We present an analysis of the 0.95–14.5 μm spectral energy distributions of nine field ultracool dwarfs with spectral types ranging from L1 to T4.5. Effective temperatures, gravities, and condensate cloud sedimentation efficiencies are derived by comparing the data to synthetic spectra computed from atmospheric models that self-consistently include the formation of condensate clouds. Overall the model spectra fit the data well, although the agreement at some wavelengths remains poor due to remaining inadequacies in the models. Derived effective temperatures decrease steadily through the L1 to T4.5 spectral types and we confirm that the effective temperatures of ultracool dwarfs at the L/T transition are nearly constant, decreasing by only ~ 200 K from spectral types L7.5 to T4.5. The condensate cloud properties vary significantly among the L dwarfs in our sample, ranging from very thick clouds to relatively thin clouds with no particular trend with spectral type. The two objects in our sample with very red $J - K_s$ colors are, however, best fitted with synthetic spectra that have thick clouds which hints at a possible correlation between the near-infrared colors of L dwarfs and the condensate cloud properties. The fits to the two T dwarfs in our sample (T2 and T4.5) also suggest that the clouds become thinner in this spectral class, in agreement with previous studies. Restricting the fits to narrower wavelength ranges (i.e., individual photometric bands) almost always yields excellent agreement between the data and models. In some cases, the models even reproduce the detailed structure of the weak H_2O and CH_4 absorption features. Limitations in our knowledge of the opacities of key absorbers such as FeH, VO, and CH_4 at certain wavelengths remain obvious, however. The effective temperatures obtained by fitting the narrower wavelength ranges can show a large scatter compared to the values derived by fitting the full spectral energy distributions; deviations are typically ~ 200 K and in the worst cases, up to 700 K. In spite of the uncertainties remaining in the models, the approach presented here works rather well and should be extended to a much larger sample.

Subject headings: infrared: stars — stars: low-mass, brown dwarfs stars: fundamental — radiative transfer

1. INTRODUCTION

The emergent spectra of very low-mass (VLM) stars and brown dwarfs, collectively known as ultracool dwarfs, are shaped in large part by gas and condensation chemistry. The low temperature ($500 \text{ K} \lesssim T \lesssim 3000 \text{ K}$), high pressure ($1 \text{ bar} \lesssim P \lesssim 10 \text{ bar}$) conditions typical of ultracool dwarf atmospheres favor the formation

of molecules (such as CO, CH_4 , N_2 , NH_3 , and H_2O) and, at $T < 2400 \text{ K}$ condensates from the refractory elements (Ti, V, Ca, Al, Fe, Si, and Mg). Condensation removes gaseous opacity sources (such as TiO, VO, FeH, CrH) from the atmosphere and alters the atmospheric chemistry as the condensates gravitationally settle and form clouds that deplete the upper layers of the atmosphere of both the condensates and their constituent elements (Fegley & Lodders 1994, 1996; Lodders 1999, 2002; Burrows & Sharp 1999). Condensates also contribute their own opacity, which can be substantial for the more abundant Fe-, Mg-, and Si-bearing species such as forsterite (Mg_2SiO_4), enstatite (MgSiO_3), and solid or liquid Fe (e.g., Marley et al. 2002; Tsuji 2002).

This rich chemistry gives rise to complex emergent spectra that are distinctly non-Planckian. The molecular line opacities dominate over all of the continuum opacity sources (e.g., H^-) that are important in the atmospheres of hotter stars (Allard & Hauschildt 1995) and as a result the emergent spectra of ultracool dwarfs exhibit strong molecular absorption bands of TiO, H_2O , and CH_4 . Indeed, it is the strength of these and other molecular bands that are used to define the L and T spectral classes (Kirkpatrick et al. 1999; Burgasser et al. 2006a). L dwarf ($2400 \text{ K} \lesssim T_{\text{eff}} \lesssim 1400 \text{ K}$) spectra exhibit weakening TiO and VO bands at red optical wavelengths (0.6–1.0 μm) due to the formation of Ti-bearing

¹ Based in part on data collected at Subaru Telescope, which is operated by the National Astronomical Observatory of Japan.

² Steward Observatory, University of Arizona, 933 North Cherry Avenue, Tucson, AZ 85721, mcushing@ifa.hawaii.edu Current address: Institute of Astronomy, University of Hawai'i, 2680 Woodlawn Drive, Honolulu, HI 96822

³ NASA Ames Research Center, MS 254-3, Moffett Field, CA 94035, Mark.S.Marley@NASA.gov

⁴ Los Alamos National Laboratory, Applied Physics Division, MS F663, Los Alamos, NM 87545, dsaumon@lanl.gov

⁵ Steward Observatory, University of Arizona, 933 North Cherry Avenue, Tucson, AZ 85721, bkelly@as.arizona.edu

⁶ SOFIA-USRA, NASA Ames Research Center MS N211-3, Moffett Field, CA 94035, wvacca@mail.arc.nasa.gov

⁷ Institute for Astronomy, University of Hawai'i, 2680 Woodlawn Drive, Honolulu, HI 96822, rayner@ifa.hawaii.edu

⁸ SETI Institute, NASA Ames Research Center, MS 254-5, Moffett Field, CA 94035, freedman@darkstar.arc.nasa.gov

⁹ Planetary Chemistry Laboratory, Department of Earth and Planetary Sciences, Washington University, St. Louis, MO, 63130, lodders@levee.wustl.edu

¹⁰ NASA Ames Research Center MS N245-6, Moffett Field, CA 94035, thomas.l.roellig@nasa.gov

condensates such as perovskite (CaTiO_3). The loss of the gaseous TiO and VO opacity results in a more transparent atmosphere and leads to the emergence of monatomic alkali lines (Na, K, Rb, Cs). Most prominent are the resonance Na I (5890/5896 Å) and K I (7665/7699 Å) doublets, which become increasingly broad with later spectral type. At near-infrared wavelengths (1–2.5 μm) the L dwarfs also become progressively redder with later spectral types due to the additional condensate opacity. As CH_4 becomes the dominant carbon-bearing gas in the upper, coolest layers of the atmosphere ($\text{CO}/\text{CH}_4 < 1$ for $T \lesssim 1100$ K at $P=1$ bar), CH_4 absorption bands emerge at near-infrared wavelengths which signals the transition between the L and T (1400 K $\lesssim T_{\text{eff}} \lesssim 700$ K) spectral classes. The K I and Na I resonance lines are present in the red optical spectra of T dwarfs (Burgasser et al. 2003a) because the high temperature condensate anorthite ($\text{CaAl}_2\text{Si}_2\text{O}_8$), a feldspar, has gravitationally settled out of the cooler atmospheric regions. In the absence of such settling, Na and K would condense into a feldspar in the form of albite ($\text{NaAlSi}_3\text{O}_8$) and orthoclase (KAlSi_3O_8) (Burrows & Sharp 1999; Lodders 1999; Marley et al. 2002).

The observed spectra and photometry of ultracool dwarfs can therefore serve as touchstones against which we can test our understanding of atmospheric physics, chemistry, dynamics, and cloud processes as embodied in our atmospheric models. Shortly after the discovery of the first bona fide brown dwarf, Gliese 229B (Nakajima et al. 1995), a number of publications appeared comparing the observed spectrum to models (Allard et al. 1996; Marley et al. 1996; Tsuji et al. 1996). Burrows et al. (2001) presented a review of the substantial subsequent work devoted to understanding the properties of L and T dwarfs. Although the comparison of models to the spectra of individual objects such as Gl 229B (Saumon et al. 2000) and Gl 570D (Geballe et al. 2001; Saumon et al. 2006) has played an important role in the progression of the field, relatively little work has been done on comparing entire classes of models to uniform datasets. Such comparisons are important as they can reveal the global properties of a set of objects and highlight the systematic strengths and weaknesses of the models.

In this work, we present such a comparison to one particular set of atmospheric models (Marley et al. 2002, 2007, in preparation). We aim to understand what the modeling has accomplished to date and to help direct future models and observations along the pathways that seem most promising. The paper is organized as follows. Sections §2 and §3 present the data and model atmospheres used in the analysis, respectively. In §4, we present the results of the comparisons between the data and models and in §5, we discuss two systematic uncertainties that affect our analysis.

2. THE DATA

There are currently eleven L and T dwarfs that have published spectra with nearly complete wavelength coverage from 0.65 to 14.5 μm (Cushing et al. 2006; Saumon et al. 2007). We selected the 5 L and 2 T dwarfs from the Cushing et al. sample with the highest S/N spectra that are not known to be multiple systems. We also included two additional L dwarfs, 2MASS

J1506514+1321060 and DENIS J025503.3–470049.0, that were not part of the Cushing et al. sample. The properties of the dwarfs in our sample, including optical and infrared spectral types and Two Micron All Sky Survey (2MASS; Skrutskie et al. 2006) photometry, are given in Table 1. Although both optical and infrared spectral types are listed in Table 1, we hereafter use optical types for the L dwarfs (Kirkpatrick et al. 1999) and infrared types for the T dwarfs (Burgasser et al. 2006a). In addition, we abbreviate the numerical portions of the 2MASS, Sloan Digital Sky Survey (SDSS; York et al. 2000), and Deep Near Infrared Survey of the Southern Sky (DENIS; Epchtein et al. 1997) target designations as hhmm±ddmm, where the suffix is the sexagesimal Right Ascension (hours and minutes) and declination (degrees and arcminutes) at J2000 equinox.

The 0.65–14.5 μm spectra used in this work were constructed from the following sources: red-optical spectra were obtained with the Low Resolution Imaging Spectrograph (LRIS; Oke et al. 1995) at the Keck telescope; near-infrared spectra were obtained with SpeX (Rayner et al. 2003) at the NASA IRTF and the Infrared Camera and Spectrograph (IRCS; Kobayashi et al. 2000) on Subaru; and mid-infrared (5.5–14.5 μm) spectra were obtained with the Infrared Spectrograph (IRS; Houck et al. 2004) on board the *Spitzer Space Telescope* (Werner et al. 2004). The only wavelengths not covered by these spectra are those containing the strong telluric absorption bands at 1.9 and 2.6 μm and the 4.5–5.5 μm range. The latter wavelength range is exceedingly difficult to observe from the ground and is not covered by the IRS. Table 2 lists both the references and resolving powers of the various spectra used in this work. For each dwarf, the different spectra were absolutely flux calibrated using ground-based photometry and then combined into a single 0.65–14.5 μm spectrum as described in Cushing et al. (2005, 2006).

Figure 1 shows the 2MASS $J-H$, $H-K_s$, and $J-K_s$ colors as a function of spectral type for all of the L and T dwarfs listed in the Dwarf Archives¹¹ web site as of 2007 June 07. The dwarfs in our sample are shown as red points. Overall, our sample is representative of dwarfs with similar spectral types. However, 2MASS 2224–0158 (L4.5) and 2MASS 0825+2115 (L7.5) have relatively red $J-K_s$ colors given their spectral types and 2MASS J1507–1627 (L5) has a relatively blue $J-K_s$ color. We discuss these dwarfs in more detail in §4.6.

3. THE MODELS

The L and T dwarf models presented here have been produced in the same way as those in our earlier work (e.g., Marley et al. 1996; Burrows et al. 1997; Marley et al. 2002; Saumon et al. 2006). We are preparing a complete description of the models for a future publication. Briefly, we computed a grid of one-dimensional, plane-parallel, hydrostatic, non-gray, radiative-convective equilibrium atmosphere models using our standard modeling code. A one-dimensional, plane parallel approximation is appropriate since the atmospheric scale height is always much smaller than the ultracool dwarf radius. We do not use mixing length theory, but rather set the local lapse rate in the con-

¹¹ <http://DwarfArchives.org>

vective regions to the adiabatic lapse rate. This is an excellent approximation in the dense, warm atmospheres of brown dwarfs and giant planets where convection is a very efficient energy transport mechanism. The superadiabaticity is very small and the atmospheric profile is insensitive to the choice of mixing length (Baraffe et al. 1997; Allard et al. 1997).

For the chemical equilibrium calculations we use the elemental abundance data of Lodders (2003) and compute compositions following Fegley & Lodders (1994), Lodders & Fegley (2002), and Lodders (1999, 2002). The chemical equilibrium abundances are computed for local thermodynamic equilibrium conditions. In stellar atmospheres, departures from thermochemical equilibrium can arise from interactions of atoms and molecules with the non-thermal radiation field while in planetary atmospheres, non-equilibrium conditions can arise from vertical transport (by convection or eddy diffusion) on a time scale shorter than that of the chemical reactions involved. In ultracool dwarf atmospheres, the first effect is negligible compared to the second. In the present work, we neglect both effects. The opacity database includes the molecular lines of H_2O , CH_4 , CO , NH_3 , H_2S , PH_3 , TiO , VO , CrH , FeH , CO_2 , HCN , C_2H_2 , C_2H_4 , and C_2H_6 , the atomic lines of the alkali metals (Li, Na, K, Rb and Cs), and continuum opacity from H_2 collision induced absorption (CIA), Rayleigh scattering from H_2 , H and He, bound-free opacity from H, H^- , and H_2^+ , and free-free opacity from He, H_2^- , and H_2^+ . The molecular line lists are continually updated and while they have well-known shortcomings, they represent the state-of-the-art. An explanation of the treatment of line broadening, and further details regarding the chemical equilibrium calculation are presented in Freedman et al. (2007). Note that we do not include a turbulent velocity in the calculation of line shapes as test calculations have shown this has a negligible effect for the temperatures and pressures considered here. An error in the TiO line opacity database (Schwenke 1998) employed in our recent generations of models (including those in Marley et al. (2002), Burgasser et al. (2002b), and Knapp et al. (2004)) that resulted in too-strong TiO absorption has been corrected.

For the model atmosphere calculation we use the k -coefficient method to describe the opacities (Goody et al. 1989). Within each of 180 spectral bins we sum the opacity arising from *each* of the several hundred million atomic and molecular lines in our database. Our radiative transfer follows the source function technique (Toon et al. 1989), allowing inclusion of arbitrary Mie scattering particles in the layer opacities. This approach is exact in the limit of single scattering and treats multiple scattering by assuming that the scattered radiation field can be approximated with two streams. After computing a pressure-temperature (P, T) profile with the k -coefficient method for a given set of parameters, we compute a high resolution spectrum by solving the monochromatic radiative transfer equation for a larger number of frequency points (typically ~ 190000 in the range of 0.4 to $50 \mu\text{m}$), using the exact same molecular line lists, continuum opacity sources, chemical composition, and line profiles as those used for the computation of the k -coefficients. The resulting spectra can be smoothed or binned for comparison with

data. Previous applications of our atmospheres code include the generation of P/T profiles and spectra for Titan (McKay et al. 1989), Uranus (Marley & McKay 1999), hot Jupiters (Fortney et al. 2005, 2006), and brown dwarfs (Marley et al. 1996; Burrows et al. 1997; Marley et al. 2002; Saumon et al. 2006).

As we converge to a model temperature-pressure profile, we compute the condensate size and vertical profiles following the prescription of Ackerman & Marley (2001) for various values of the cloud sedimentation efficiency parameter, f_{sed} . Larger values of f_{sed} imply larger particle sizes and thus greater sedimentation efficiency. The width of the lognormal particle size distribution is set at $\sigma = 2$ and the eddy diffusion coefficient above the convective region is set to $K_{\text{zz}} = 10^5 \text{ cm}^2 \text{ sec}^{-1}$. This latter value is consistent with that found from studies of the effect of non-equilibrium chemistry in L and T dwarf atmospheres (Saumon et al. 2006; Leggett et al. 2007). For any P/T profile there is a single description of the variation in particle sizes and number densities with altitude for each of the condensed species. As the atmospheric structure is iterated towards the equilibrium solution the cloud description is also continuously updated. The final result is a single, self-consistent thermal and cloud profile with the specified gravity, effective temperature, and cloud sedimentation efficiency. We term these models ‘cloudy’. We also consider models in which the condensate formation is included in the chemical equilibrium calculation, but the condensate opacity is neglected. We term these models ‘clear’ and denote them as $f_{\text{sed}}=\text{nc}$, since the models include ‘no cloud’ opacity.

In this first study, for the sake of simplicity, we consider a model parameter space consisting of T_{eff} , g , and f_{sed} at solar metallicity. A more extensive study including variations in metallicity and the other cloud parameters, as well as departures from chemical equilibrium caused by vertical mixing in the atmosphere (e.g. Saumon et al. (2006)), will be the subject of future papers. Evolutionary models predict that field L and T dwarfs with ages greater than a few hundred million years have $700 \text{ K} \lesssim T_{\text{eff}} \lesssim 2400 \text{ K}$ and $5.0 \lesssim \log g \text{ (cm s}^{-2}\text{)} \lesssim 5.5$ (Burrows et al. 1997). We consider the entire range of T_{eff} in steps of 100 K, and values of $\log g$ of 4.5, 5.0, and 5.5. In previous work found that $f_{\text{sed}} \sim 3$ best reproduces global properties of Jupiter’s ammonia cloud (Ackerman & Marley 2001) and the $J - K$ colors of L dwarfs (e.g., Knapp et al. 2004). However the excess TiO opacity in our previous models, particularly in the J band, may have led us to overestimate the f_{sed} value for L dwarfs. Accordingly here we consider models with $f_{\text{sed}}=1, 2, 3, 4$, and nc. The final grid contains 270 models.

Dynamical processes in the atmospheres of individual objects ultimately control the growth and sedimentation of condensates and the optical properties of the various cloud decks expected in these atmospheres (e.g., Helling et al. 2001; Woitke & Helling 2003, 2004; Helling et al. 2004; Helling & Woitke 2006). Although our modeling parameter, f_{sed} aims to self-consistently capture these processes in a tractable way, the global properties of each individual object must ultimately define the true properties of the clouds. However we do not yet understand how differences in metallicity, rotation rate, effective temperature, and gravity might manifest

themselves as different values of f_{sed} . Therefore while we treat this parameter on equal footing as g and T_{eff} for fitting purposes, we recognize that ultimately, more complete models would find that f_{sed} is determined by the global physical properties of individual objects.

For each combination of gravity, effective temperature, and sedimentation efficiency, we compute a self-consistent atmospheric temperature-pressure profile. Using this profile and employing the same atmospheric chemistry and opacities, we compute a high resolution synthetic spectrum. This spectrum is then smoothed to the resolving power of the data using a Gaussian kernel and resampled onto the same wavelength grid. Figures 2 and 3 show a sequence of synthetic spectra, smoothed to $R=500$ for clarity, with atmospheric parameters typical of an L dwarf ($T_{\text{eff}}=1800$ K, $\log g=5.0$, $f_{\text{sed}}=2$) and a T dwarf ($T_{\text{eff}}=1100$ K, $\log g=5.0$, $f_{\text{sed}}=\text{nc}$). The three panels in each figure illustrate the variations in spectral morphology when just one of the three parameters is changed.

The upper panels show the changes in spectral morphology due to variations in T_{eff} at a fixed g and f_{sed} . With decreasing T_{eff} , the L dwarfs (Fig. 2) become redder in the near-infrared and the depths of the H_2O bands become deeper. Note also that the Q branch of the ν_3 fundamental band of CH_4 at $3.3 \mu\text{m}$ is present at $T_{\text{eff}}=1700$ K. The depths of the H_2O , CH_4 , and NH_3 bands in the spectra of the T dwarfs (Fig. 3) become deeper with decreasing T_{eff} but in contrast to the L dwarfs, the T dwarfs become slightly bluer in the near-infrared.

The middle panels show the changes in spectral morphology due to variations in g at a fixed T_{eff} and f_{sed} . In the L dwarfs the primary effect of increasing g is to weaken the near-infrared H_2O absorption bands. At these temperatures, the molecular abundance of H_2O and CH_4 depend weakly on the atmospheric pressure and are thus not sensitive to changes in gravity. The change in the H_2O band strengths is instead a result of the fact that, at a given pressure level in the atmosphere, the higher gravity models are cooler and as a result have thicker condensate clouds. The clouds produce a grayer emergent spectrum and are therefore responsible for the decreased depth of the H_2O bands. In contrast to the L dwarfs, the H_2O and CH_4 band depths in the spectra of T dwarfs are only marginally affected by changes in g , except in the K band. The peak flux level in the K band diminishes with increasing g due to an increase in the CIA of H_2 . This broad, featureless absorption band (e.g., Borysow et al. 1997) centered at $2.4 \mu\text{m}$ is very sensitive to atmospheric pressure, and thus g , since it involves the collisions of particles ($\kappa_\nu \propto n_{\text{gas}}^2$, where n_{gas} is the number density of the gas).

Finally, the lower panels show the changes in spectral morphology due to variations in the cloud sedimentation parameter f_{sed} at a fixed T_{eff} and g . Changes in f_{sed} produce the most dramatic variations in spectral morphology (particularly in the $1\text{--}6 \mu\text{m}$ region) underscoring the importance of correctly modeling the formation and subsequent sedimentation of condensates. The additional condensate opacity results in emergent spectra that are redder at near-infrared wavelengths than those from the cloudless models ($f_{\text{sed}}=\text{nc}$). The impact of the

clouds on the emergent spectra of ultracool dwarfs becomes more dramatic with lower f_{sed} values because the clouds are thicker and thus contribute more opacity to the atmosphere.

4. ATMOSPHERIC PARAMETERS OF L AND T DWARFS

4.1. Fitting Technique

The 1D model atmospheres predict the emergent flux density \mathcal{F}_ν ($\mathcal{F}_\nu = 2\pi \int_0^\infty I_\nu \mu d\mu$) as a function of wavelength (i.e., a synthetic spectrum) at the surface of a star. The synthetic spectra must be multiplied by $(R/d)^2$, where R is the stellar radius and d is the stellar distance, in order to obtain fluxes at Earth and directly compare them to observations. Although the parallaxes of nearly 80 L and T dwarfs have been measured (e.g., Dahn et al. 2002; Tinney et al. 2003; Vrba et al. 2004; Costa et al. 2006), the radii of field L and T dwarfs are currently unknown. Therefore we can compare only the relative shapes of the modeled spectral energy distributions (SEDs) to the data.

For each model k , which hereafter is denoted by the triplet $[T_{\text{eff}}/\log g/f_{\text{sed}}]$, we compute a goodness-of-fit statistic G_k defined by¹²,

$$G_k = \sum_{i=1}^n w_i \left(\frac{f_i - C_k \mathcal{F}_{k,i}}{\sigma_i} \right)^2, \quad (1)$$

where n is the number of data pixels, w_i is the weight for the i th wavelength, f_i and $\mathcal{F}_{k,i}$ are the flux densities of the data and model k , respectively, σ_i are the errors in the observed flux densities, and C_k is the unknown multiplicative constant equal to $(R/d)^2$. For each model k , the constant C_k is determined by minimizing G_k with respect to C_k and is given by,

$$C_k = \frac{\sum w_i f_i \mathcal{F}_{k,i} / \sigma_i^2}{\sum w_i \mathcal{F}_{k,i}^2 / \sigma_i^2}. \quad (2)$$

We select the best fitting synthetic spectrum by locating the global minimum of the G values for all of the model spectra in our grid.

We have no *a priori* reason to favor one wavelength range over another and therefore, in principle, all wavelengths points could receive equal weight in our fits. However given the large variation in the wavelength sampling of our data (e.g, the near-infrared spectra cover only $\sim 2 \mu\text{m}$ but have ~ 20 times more wavelength points than the *Spitzer* IRS spectra which cover $\sim 10 \mu\text{m}$), G would be heavily biased towards near-infrared wavelengths if w_i was set to unity for all i . We therefore chose to weight each pixel by its width in microns ($w_i = \Delta\lambda_i$). In §5.2, we discuss the systematic effects that our choice of weights has on our results. Since the line lists of CH_4 are incomplete in the H -band (Burrows et al. 2001; Freedman et al. 2007), and the $E^4\Pi - A^4\Pi$ system

¹² We also tested the usefulness of the statistic $G_k = \sum_{i=1}^n w_i \left(\frac{f_i - C_k \mathcal{F}_{k,i}}{f_i} \right)^2$ since most published spectra do not have errors associated with the flux density values. However as noted by Takeda (1995), such a statistic gives more weight to wavelengths with low flux values. Typically ultracool dwarf spectra have very low S/N at such wavelengths and thus care must be taken when using such a statistic.

of FeH at 1.6 μm which is present in the spectra of the L dwarfs (Wallace & Hinkle 2001; Cushing et al. 2003) lacks a line list, we also set the weights of the pixels from 1.58 to 1.75 μm (roughly the center of the *H* band) to zero.

As an example of our procedure, Figure 4 shows the G values of all the synthetic spectra in our grid as a function of T_{eff} computed for the spectrum of 2MASS 1507–1627 (L5). In this case, the best fitting synthetic spectrum has the parameters [1700/4.5/2]. However there are additional synthetic spectra that yield similar minimum G values. How then can we determine the quality of a given fit? Although G is mathematically similar to the χ^2 statistic, it does not follow a χ^2 distribution¹³ and as a result, we cannot employ standard hypothesis testing techniques to assess the quality of the fits.

We therefore performed a Monte Carlo simulation to determine the range of synthetic spectra that fit the data given the observational errors. For each observed spectrum, we generated 2000 simulated data sets wherein the flux at each wavelength point was randomly drawn from a Gaussian distribution centered on the observed flux, and with a width given by the observed variance in the individual pixel. Since each 0.65–14.5 μm spectrum was constructed by combining together spectra that were absolutely flux calibrated independently, the error in any given flux density value also includes a correlated component that arises from the fact that during the absolute flux calibration process, all of the flux density values over a range of wavelengths (e.g., 1–2.5 μm) are scaled by a constant to adjust the overall flux level to match broadband photometry. We therefore scale the simulated flux density values by $10^{-0.4 \times K}$ where K is randomly drawn from a Gaussian distribution centered on zero, and with a width given by the variance of the photometry (in magnitudes).

A simulated data set s_i is constructed from m spectra, each having its own σ_{ph}^2 . For a given spectrum j , the simulated dataset s_i is given by,

$$s_i = \mathcal{N}(f_i, \sigma_i^2) 10^{-0.4 \times \mathcal{N}(0, \sigma_{ph,j}^2)}, \quad (3)$$

where $\mathcal{N}(\mu, \sigma^2)$ represents a value randomly drawn from a Gaussian distribution with mean μ and variance σ^2 , and $\sigma_{ph,j}^2$ is the variance of the photometry used to absolutely flux calibrate the spectrum j . We then replace f_i with s_i in Equations 1 and 2 and recompute the best fitting synthetic spectrum. The quality of the fit between the data and a given synthetic spectrum is given by f_{MC} , the fraction of the 2000 simulations in which the given synthetic spectrum is identified as the best fitting spectrum. In the case described above, the synthetic spectrum with the parameters [1700/4.5/2] has $f_{\text{MC}}=1.000$ and thus is the best representation of the data in our grid of synthetic spectra. Values of f_{MC} much less than unity imply that more than one synthetic spectrum in the grid fits the data well.

¹³ The χ^2 distribution with ν degrees of freedom is defined to be the sum of ν squared standard normal deviates or $\chi_\nu^2 = \sum z_i^2$, where $z_i = (x_i - \mu)/\sigma_i$. Since the models are known to have systematic errors, the standardized residuals $z_i = (f_i - C_k \mathcal{F}_{k,i})/\sigma_i$ are not standard normal deviates and thus G does not follow a χ^2 distribution.

The best fitting model parameters are given on the model grid points without interpolation. Nominally, this would give an internal uncertainty of half of the grid spacing, or ± 50 K in T_{eff} , ± 0.25 in $\log g$, and ± 0.5 in f_{sed} . In practice, the best fitting models nearly all have $f_{\text{MC}} \sim 1$, which shows that the internal uncertainties on the fitting parameters are even smaller than those nominal values. As we will see in §5, our fits of the ultracool dwarf SEDs are affected by systematic effects that dominate the internal uncertainties and that are difficult to quantify. In addition, changes in the models (e.g., the inclusion of [Fe/H] as an additional parameter) or the use of a different goodness-of-fit statistic could yield different atmospheric parameters than we find here. An accurate determination of physical parameters of ultracool dwarfs will therefore require the development of more complete model atmospheres. Nonetheless, trends in the fitted parameters as revealed by this work should improve our understanding of the physics of ultracool dwarfs.

4.2. Fits of the Entire SED

We fit 0.95–14.5 μm spectrum of each dwarf as described in the previous section. Although the data extend blueward to 0.65 μm , the analysis was limited to wavelengths greater than 0.95 μm because the pressure-broadened wing of the resonant K I doublet (7665, 7699 Å) that extends to ~ 0.9 μm is exceedingly difficult to model (Burrows & Volobuyev 2003). Table 3 lists the best fitting model parameters (T_{eff} , $\log g$, f_{sed}) for each dwarf in our sample along with the fraction of the Monte Carlo simulations (f_{MC}) in which the given triplet was identified as the best fitting model. All models with $f_{\text{MC}} > 0.1$ are listed. A summary of the derived parameters is shown in Figure 5. Seven of the nine dwarfs in our sample have best fitting synthetic spectra with $f_{\text{MC}} \sim 1$ indicating that they are the only reasonable model spectra in our grid for these dwarfs. 2MASS 1439+1929 (L1) has two model spectra that differ by 1 in f_{sed} with nearly equal f_{MC} values while SDSS 1254–0122 (T2) has two models with $f_{\text{MC}} > 0.1$ that differ by 0.5 dex in $\log g$ and 1 in f_{sed} .

The derived T_{eff} values decrease steadily with later spectral type but the difference in T_{eff} between 2MASS 0825+2115 (L7.5) and 2MASS 0559–1404 (T4.5) is only 200 K which confirms that the transition between the L and T dwarfs occurs over a narrow range in T_{eff} as has been noted previously (e.g., Kirkpatrick et al. 1999; Burgasser et al. 2002a; Golimowski et al. 2004). Golimowski et al. (2004) derive the effective temperatures of ~ 40 L and T dwarfs using their observed bolometric luminosities and evolutionary models (see Dahn et al. (2002), Vrba et al. (2004), and Basri et al. (2000) for alternative T_{eff} scales for L and T dwarfs). Seven of these dwarfs are included in our sample so we also show in Table 3 the Golimowski et al. T_{eff} values for ages of 0.1, 3, and 10 Gyr. The agreement between the two sets of values is excellent as all of our derived values fall within their 0.1 to 10 Gyr ranges.

The comparison of our derived T_{eff} values with those of Golimowski et al. implies that if they are single objects, seven of nine dwarfs in our sample are much younger than 3 Gyr. Our evolutionary calculations (Marley et al. 2007, in preparation) also indicate that if we take the derived

T_{eff} and g values at face value, five of the L dwarfs would be younger than 0.2 Gyr. This is primarily a consequence of the low gravities obtained from fitting the SEDs. It seems unlikely that our sample would be biased towards such young ages given that the mean age of the L and T dwarf field population is several Gyr (Dahn et al. 2002; Allen et al. 2005). This suggests that fitting the SEDs of ultracool dwarfs is a poor method to determine gravities. Fortunately, we can obtain the gravity using an alternate method.

When the parallax of an object is known, its radius can be determined using the fitted normalization constant (Eq. 2) since $C_k=(R/d)^2$. With ultracool dwarf evolution sequences, (T_{eff},R) values can be transformed uniquely into (T_{eff},g) values. The gravities obtained with this alternate method are given in Table 3 and are shown in blue in the upper panel of Figure 5. The scatter in $\log g$ is reduced and nearly all gravities are above $\log g=5.0$. Our evolution sequences show that all 9 objects now have ages above 0.3 Gyr. This alternate method only weakly depends on the relatively subtle variations in spectral morphology arising from changes in g (Fig. 2 and 3) because it relies primarily on fitting the absolute flux level of the SED. The reduced scatter in $\log g$ and the older age distribution of our sample indicate that the method provides gravity estimates that are more reliable than those obtained by direct spectral fitting. Hereafter, we do not compute new model atmospheres with these new gravities but rather continue to compare the data to models in our grid with $\log g=4.5, 5.0, \text{ and } 5.5$.

We also note that the theoretical evolution of ultracool dwarfs with cloudy atmospheres is limited to $\log g \leq 5.38$, although the evolution with cloudless atmospheres can reach slightly higher gravities of $\log g \sim 5.48$. Because the mass- T_{eff} -radius relation of brown dwarfs is well established on theoretical grounds, it provides a firm boundary to physically plausible combinations of T_{eff} and g . We find that the $\log g$ values of three of our objects (derived using the alternate method) exceed the limit for ultracool dwarfs with cloudy atmospheres, which is an indication that their fitted T_{eff} values are overestimated by $\sim 10\text{--}20$ K. This result can be understood by noting that the gravity of brown dwarfs is a very sensitive function of T_{eff} for a fixed L_{bol} (see, for example, Fig. 1 of Saumon et al. (2006)). This is a consequence of the mass-radius relation for degenerate stars where $R \sim M^{-1/3}$. Since $L_{\text{bol}} \sim R^2 T_{\text{eff}}^4$, it follows that at constant L_{bol} , $g \sim T_{\text{eff}}^{10}$. From this approximate relation, a 7% variation in T_{eff} changes the gravity by 0.3 dex.

Two objects in our sample call for a more detailed discussion. SDSS 1254–0122 (T2) and especially 2MASS 0559–1404 (T4.5) stand out as being overluminous for their spectral types (Burgasser 2007). It has therefore been suggested that the two objects may be unresolved binaries (Golimowski et al. 2004; Vrba et al. 2004; Liu et al. 2006; Burgasser 2007), although neither dwarf has been resolved into a binary in high-resolution imaging (Burgasser et al. 2003b, 2006b). We find, as did Golimowski et al. (2004), that the two objects share essentially the same T_{eff} , although we derive $T_{\text{eff}}=1200$ K while Golimowski et al. find $T_{\text{eff}}=1475$ K (assuming ages of 3 Gyr). If SDSS 1254–0122 and 2MASS 0559–1404 are equal magnitude binaries, then the L_{bol}

of each component is reduced by a factor of two and the Golimowski et al. T_{eff} value becomes ~ 1200 K which is in much better agreement with our value. Given these new parameters, our evolutionary sequences provide the corresponding properties for the individual components. To satisfy both the constraints of component luminosity and the maximum allowed gravity, T_{eff} has to be reduced slightly, but remain within the uncertainties of our spectral fits. The properties of the individual components are given in Table 4.

Whether SDSS 1254–0122 and 2MASS 0559–1404 are singles or equal mass binaries, they have essentially the same effective temperature. The difference in the appearance of their spectra (T2 versus T4.5), can be explained as primarily due to a difference in their cloud properties, as suggested by our fits that indicate the clouds are thinner (larger f_{sed}) in 2MASS 0559–1404 than in SDSS 1254–0122. Another possibility would be for SDSS 1254–0122 to be a single brown dwarf (or a strongly unequal-mass binary) and for 2MASS 0559–1404 to be an equal mass binary. This would make the latter’s individual components less luminous than SDSS 1254–0122 (or its primary) and is consistent with their position in the M_{bol} vs spectral type diagram (Burgasser 2007).

A fair amount of scatter is found in the f_{sed} values of the L dwarfs, with an indication that f_{sed} increases toward the later T spectral class, as would be expected if clouds play a decreasing role in shaping the SED of T dwarfs (e.g., Marley et al. 2002; Burrows et al. 2006). Among the L dwarfs in our sample, f_{sed} ranges from 1 to 3, implying that the cloud opacity varies appreciably among L dwarfs (bottom panel of Fig. 2) with little, if any, dependence on the spectral type. It would be particularly interesting to establish the distribution of f_{sed} as a function of spectral type with a larger sample.

Figure 6 shows the 0.95–14.5 μm spectra of 2MASS 1439+1929 (L1), 2MASS 0036+1821 (L3.5), 2MASS 1507–1627 (L5), DENIS 0255–4700 (L8), SDSS J1254–0122 (T2), and 2MASS 0559–1404 (T4.5) along with the best fitting model spectra. The grey regions indicate wavelength ranges that were excluded from the fits. The models fit the data reasonably well at the earliest and latest spectral types, but do a poorer job of fitting the data in the mid- to late-type L dwarfs and the early-type T dwarf. This range of spectral types corresponds to the L/T transition where condensate clouds have their largest impact on the SED of ultracool dwarfs. The relatively poor fits at the L/T transition most likely reflects the limitations of our simple cloud model.

In particular, the best fitting model spectra match both the peaks and depths of the H_2O bands centered at 1.4, 1.9, and 2.6 μm well. The models do, however, underestimate the K -band flux density levels of 2MASS 1439+1929 (L1) and 2MASS 0036+1821 (L3.5). In addition, the models also over estimate the depth of the L -band CH_4 absorption bands of both DENIS 0255–4700 (L8) and SDSS 1254–0122 (T2) as well as the 5.5–14.5 μm flux levels of DENIS 0255–4700 (L8). We defer discussion of the possible causes of these mismatches to §4.3. Finally, the poor match between the model spectrum and data of 2MASS 0559–1404 in the H band is a result of the woefully incomplete line list of CH_4 at these wavelengths (Burrows et al. 2001; Freedman et al. 2007).

4.3. Description of Individual Bands

In the following sections, we describe how well the best fitting synthetic spectra match the data over narrower wavelength ranges. Figures 7 to 12 show the same data and model spectra presented in Figure 6 but over the wavelengths covered by the photometric bandpasses *Y*, *J*, *H*, *K*, and *L* and the Short-Low module of the IRS on board *Spitzer* (hereafter IRS/SL). Although the most prominent features in the spectra of the L and T dwarfs are briefly described in each section, more detailed descriptions can be found elsewhere (Kirkpatrick et al. 1999; Burgasser et al. 2003a; McLean et al. 2003; Cushing et al. 2005, 2006).

4.3.1. The *Y* Band

Figure 7 shows the spectra and best fitting models over the wavelength range 0.95 to 1.1 μm , which roughly corresponds to the *Y* band (Hillenbrand et al. 2002). The spectra of the L dwarfs are dominated by absorption features arising from the 0–0 band of the $F^4\Delta - X^4\Delta$ system of FeH. The strongest FeH feature is the bandhead at 0.9896 μm but weak FeH features are seen in the spectra of the L dwarfs throughout this wavelength range. The 0–0 band of the $A^4\Pi - X^4\Sigma^-$ system of VO centered at $\sim 1.06 \mu\text{m}$ is also present in the spectra of the early-type L dwarfs and the FeH bandhead at 0.9896 μm is weakly present in the spectra of SDSS J1254–0122 (T2) and 2MASS 0559–1404 (T4.5). Finally, H₂O and CH₄ bands at $\lambda > 1.09 \mu\text{m}$ emerge at the L/T transition and strengthen through the T sequence.

The synthetic spectra fit the overall shape of the *Y*-band spectra of the L and T dwarfs reasonably well. In particular, they match the strengths of the H₂O and CH₄ bands in the T dwarf spectra at $\lambda > 1.08 \mu\text{m}$. However there are a number of mismatches worth noting. Firstly, the FeH bandhead in the synthetic spectra is systematically weaker than in the L dwarf data. Secondly, all of the synthetic spectra exhibit the 0–1 bandhead of the $A^6\Sigma^+ - X^6\Sigma^+$ system of CrH at 0.9969 μm . This bandhead is often identified in the spectra of L dwarfs (e.g., Kirkpatrick et al. 1999; Kendall et al. 2006) but Cushing et al. (2003) questioned these identifications given that many of the absorption features at this wavelength in $R=2000$ spectra can be associated with FeH. Reiners & Basri (2006) recently found that no CrH absorption features can be identified in high resolution ($R=31,000$) spectra of M and L dwarfs which indicates that CrH is not a significant absorber at these wavelengths. Therefore the presence of this bandhead in the synthetic spectra is inconsistent with the observations. The 0–1 bandhead of the ϕ system of TiO (Galehouse et al. 1980) at $\sim 1.104 \mu\text{m}$ is also too strong in all of the model spectra. The T dwarf models exhibit a broad, weak VO band centered at $\sim 1.06 \mu\text{m}$. Observationally, this band peaks in strength at a spectral type of $\sim L5$ and is absent by a spectral type of L8 (Cushing et al. 2005) so the presence of this band in the models is also inconsistent with the observations. Finally, the best fitting model spectrum underestimates the peak flux of the T4.5 dwarf 2MASS 0559–1404 because of the presence of the condensate opacity ($f_{\text{sed}}=4$). A cloudless model would match the overall shape of the *Y* band better (see §4.4.1).

4.3.2. The *J* Band

Figure 8 shows the spectra and best fitting model spectra from 1.1 to 1.34 μm . This wavelength range contains the most prominent atomic features in the infrared spectra of L and T dwarfs, namely the two K I doublets at $\sim 1.17 \mu\text{m}$ and $\sim 1.24 \mu\text{m}$, and the Na I doublet at 1.14 μm . The 0–1 and 1–2 bands of the $F^4\Delta - X^4\Delta$ system of FeH are also present in the *J*-band spectra of the L dwarfs. These two bands exhibit bandheads at 1.1939 and 1.2389 μm , respectively, along with numerous additional weak features from 1.2 to 1.3 μm . The $3\nu_3$ and $\nu_2 + 2\nu_3$ bands of CH₄ centered at ~ 1.15 and $\sim 1.4 \mu\text{m}$ are also seen in the spectra of the T dwarfs.

The model spectra reproduce the depths of the H₂O bands at $\lambda > 1.32 \mu\text{m}$, the onset of the CH₄ absorption in the spectra of the T dwarfs, and the weakening and eventual disappearance of the Na I doublet at 1.14 μm with later spectral type. However the model spectra do a poor job of matching the peak flux levels at $\sim 1.3 \mu\text{m}$ of 2MASS 1439+1929 (L1), 2MASS 1507–1627 (L5), and 2MASS 0559–1404 (T4.5). In addition, the bandheads and other weak FeH features observed in the *J*-band spectra of the L dwarfs are completely absent from the models. This behavior mirrors that in the *Y*-band for which the FeH band is systematically weaker in the models than in the data. The cross-sections of the 0–1 and 1–2 μm FeH bands are an order of magnitude smaller than those of the 0–0 FeH band (Dulick et al. 2003) so it is not surprising that they are either very weak or absent in the synthetic spectra.

The models also are a poor match to the early-type L dwarfs near the 1.177 μm K I line since the red wing appears much too broad given the observations. This apparent line broadening in the model spectra is actually due to the presence of the 0–1 band of the $A-X$ system of VO (Cheung et al. 1982). Although this band has been identified in the spectra of young, low-gravity brown dwarfs (McGovern et al. 2004), it has not been found in the spectra of field L and T dwarfs and therefore its presence in the model spectrum implies the opacity of this VO band may be in error.

4.3.3. The *H* Band

Figure 9 shows the spectra and best fitting synthetic spectra over the 1.4 to 1.8 μm wavelength range. The L dwarf spectra are shaped primarily by H₂O absorption but also exhibit numerous weak absorption features, including three bandheads, from 1.59 to 1.74 μm that arise from the $E^4\Pi - A^4\Pi$ system of FeH. The $2\nu_3$ and $2\nu_2 + \nu_3$ bands of CH₄ appear at the L/T transition and strengthen through the T sequence. As explained in §4.1, we do not include the 1.58 to 1.75 μm wavelength range in the fits because the FeH band lacks a line list and the CH₄ line list is incomplete.

The model spectra fit the overall shape of the data reasonably well at these wavelengths. In particular, the detailed structure of the H₂O bands at the short and long wavelength ends of the *H* band are well matched by the model spectra. The best agreement between the data and model spectra at these wavelengths are obtained for DENIS 0255–4700 (L8) and SDSS 1254–0122 (T2) because the FeH band is either weak or absent from the data and only weak CH₄ absorption is present. This in-

indicates that the H₂O opacity tables are quite good in the *H* band.

4.3.4. The *K* Band

Figure 10 shows the data and best fitting synthetic spectra over the 1.9 to 2.4 μm wavelength range. The spectra of L and T dwarfs are shaped primarily by H₂O, CO, and CH₄ bands at these wavelengths. At the earliest spectral types, CO is the dominant carbon bearing gas and therefore the $\Delta\nu = +2$ CO overtone bands at $\lambda \gtrsim 2.29 \mu\text{m}$ are strong. These CO bands weaken and disappear with later spectral type as CH₄ becomes the dominant carbon-bearing gas. Additionally there is a Na I doublet at 2.26 μm present in the early-type L dwarfs.

With the exception of 2MASS 1507–1627 (L5) and 2MASS 0559–1404 (T4.5), the models are a poor fit to the *K*-band spectra. The models underestimate the *K*-band flux levels of the 2MASS J1439+1929 (L1) and 2MASS 0036+1821 (L3.5) and overestimate the strengths of the CH₄ band in DENIS 0255–4700 (L8) and SDSS J1254–0122 (T2). In addition, a weak CH₄ feature can be seen in the synthetic spectrum of 2MASS 0036+1821 (L3.5) at $\sim 2.2 \mu\text{m}$ that is not observed in spectra of ultracool dwarfs until a spectral type of \sim L8. The presence of this CH₄ feature in the model spectrum of 2MASS 0036+1821 is a result of the fact that $f_{\text{sed}}=3$ for this model. For a comparison, the best fitting model for 2MASS 1507–1627 (L5) has the same T_{eff} , but $f_{\text{sed}}=2$, and shows no CH₄ feature (the change in g makes little difference in the strength of the CH₄ band at this T_{eff}). The $f_{\text{sed}}=3$ model is cooler in the CH₄ band formation region resulting in a higher CH₄ abundance and a deeper absorption band.

As described in §3, H₂ CIA is an important pressure-sensitive opacity source in the atmospheres of ultracool dwarfs. Compared to the absorption of other molecules, (primarily H₂O and CH₄), H₂ CIA is most significant in the *K* band. A lower metallicity decreases the opacity of H₂O and CH₄ relative to the H₂ CIA continuum, which results in stronger emission in the *Y*, *J* and *H* bands with respect to the *K* band (Burgasser et al. 2002a). In previous work (Saumon et al. 2006, 2007), we found that our solar metallicity models systematically underestimated the *K*-band fluxes of late-type T dwarfs while models with $[\text{Fe}/\text{H}] = +0.3$ fit the *K*-band peak well. Therefore the poor match between the data and model spectra in the *K* band may indicate that the metallicities of the L and T dwarfs in our sample differ somewhat from the solar value employed in our chemical equilibrium calculations. Another possibility that explains the mismatch between the spectra DENIS 0255–4700 (L8) and SDSS 1254–0122 (T2) and the best fitting models is the cloud properties since the cloud sedimentation efficiency f_{sed} changes from 2 to 3 to 4 from L8 to T4.5.

4.3.5. The *L* Band

Figure 11 shows the spectra and best fitting synthetic spectra over the 3.0 to 4.1 μm wavelength range. The spectra are dominated by weak H₂O features and the ν_3 fundamental band of CH₄. The Q-branch ($\sim 3.3 \mu\text{m}$) is the first CH₄ feature to emerge in the spectra of the L dwarfs and does so at a spectral type of \sim L5. With increasing spectral type, the P and the R branches emerge

and strengthen through the spectral sequence until the band is saturated in the late-type T dwarfs.

The model spectra do not match the data particularly well in the *L* band. The most egregious mismatch is 2MASS 0036+1821 (L3.5) for which the model shows a very strong CH₄ band that is absent in the data. The presence of the CH₄ band is due to the fact that the best fitting model has $f_{\text{sed}}=3$, as in the *K* band (see §4.3.5). The average flux density levels of the models also appear low for 2MASS 1507–1627 (L5), DENIS 0255–4700 (L8), SDSS J1254–0122 (T2), and 2MASS 0559–1404 (T4.5). In addition, the model for 2MASS J0559–1404 does not match the peak of the observed spectrum at $\sim 4.1 \mu\text{m}$. Generally, in objects where the CH₄ absorption is too strong in the *L* band, a corresponding mismatch occurs in the *K* and IRS/SL bands (L8 and T2). The line lists for both H₂O and CH₄ are reasonably complete at these wavelengths so the most likely explanation for the mismatch is that the region of the model atmosphere from which the *K* and *L* band and IRS/SL flux emerges is too cool, possibly as a result of the condensate cloud model.

4.3.6. IRS/SL

Figure 12 shows the data and best fitting models over the 5.5 to 14.5 μm wavelength range covered by the Short-Low module of the IRS (Houck et al. 2004). H₂O absorption features arising from the ν_2 fundamental band and $2\nu_2 - \nu_2$ overtone band are present throughout this wavelength range; the break in the spectra at 6.5 μm is an H₂O feature. The ν_4 fundamental band of CH₄ centered at $\sim 7.65 \mu\text{m}$ emerges in the spectra of late-type L dwarfs and the ν_2 fundamental band of NH₃ centered at $\sim 10.5 \mu\text{m}$ appears in the spectra of the T dwarfs.

With the exception of 2MASS 0036+1821 (L3.5), the synthetic spectra match the data reasonably well. In particular, the strengths of the H₂O band at 6.5 μm , and the CH₄ band at 7.8 μm is well matched by the model spectra. The flux level of the synthetic spectrum of DENIS 0255–4700 (L8) is low however, and there is a slight mismatch between the model spectrum and 2MASS 1507–1627 (L5) at $\sim 9 \mu\text{m}$ that we discuss further in §4.4.5. The mismatch between the model and the spectrum of 2MASS 0036+1821 is due to the fact that the model has $f_{\text{sed}}=3$ (see §4.3.4 and §4.3.5).

4.4. Fits to Individual Photometric Bands

The L and T dwarf spectra studied herein cover a broad range of wavelengths while most published spectra cover only the red optical and near-infrared wavelengths (e.g., Cruz et al. 2003; Knapp et al. 2004) or even a single photometric band (e.g., Neuhäuser et al. 2005; Metchev & Hillenbrand 2006). It is therefore appropriate to investigate how well the atmospheric parameters of L and T dwarfs can be determined by fitting L and T dwarf spectra over narrower wavelength ranges. In addition, we can also estimate the systematic errors in both the models and spectral fitting procedure by comparing how well the models fit the spectral features over narrower wavelength ranges as compared to the global 0.95–14.5 μm fits.

We therefore fit the data over the wavelength ranges described in §4.3 as well as over the 0.95–2.5 μm wave-

length range. For the IRS/SL and Y -, J -, K -, and L -band fits, we set $w_i=1$ for all i . Table 5 lists the results of the fits and Figure 13, which is similar to the lower panel of Figure 5, shows the corresponding T_{eff} values for each dwarf. Figures 14–16 and 18–20 show the spectra and best fitting models (*blue*) along with the best fitting models obtained by fitting the 0.95–14.5 μm (*red*, same as Fig. 6).

As expected, the model spectra fit the data much better over these narrower wavelength ranges. In most cases, remarkably good fits are obtained. However, the T_{eff} values derived from narrower wavelength ranges do not agree with those derived by fitting the 0.95–14.5 μm SEDs. Particularly poor T_{eff} values are derived by fitting the L band and IRS/SL spectra of the early- to mid-type L dwarfs (see Figure 13). Below, we describe how the model spectra fit the data over the narrower wavelength ranges in more detail. Since the majority of the H band is not included in the fitting process, (see §4.1), we do not present a detailed description of that wavelength region below.

4.4.1. Y Band Fits

Figure 14 shows the spectra and best fitting model spectra over the Y band. The fits reproduce the overall shape of the Y band data considerably better than 0.95–14.5 μm fits for all spectral types. The remaining discrepancies highlight problems with specific molecular bands. The model FeH bandheads at 0.9896 μm are still too weak, the 0.8611 μm CrH bandheads are still present, and the TiO bandheads at ~ 1.104 μm are still too strong. Indeed the CrH bandhead is present in all the model spectra shown in Figure 14. The strength of the ~ 1.06 μm VO band is, however, much better matched when fitting the Y band data alone. The peak flux of 2MASS 0559–1404 (T4.5) is also better matched when fitting the Y band data alone but the synthetic spectrum does exhibit the VO band that is absent from the data.

As shown in Figure 13, six of the nine dwarfs have derived T_{eff} values that fall within the Golimowski et al. (2004) effective temperature range. However the derived T_{eff} values for the early- to mid-type L dwarfs (L1 to L5) differ by no more than 200 K while the Golimowski et al. (2004) 3-Gyr effective temperatures and the T_{eff} values derived by fitting the 0.95–14.5 μm spectra vary by 500 K over the same spectral type range which indicates the Y band is not a sensitive indicator of effective temperature at these spectral types.

4.4.2. J Band Fits

Figure 15 shows the spectra and best fitting models over the 1.1 to 1.34 μm wavelength range. Fits to the J -band spectra alone significantly improve for those dwarfs where the global fit was rather poor, i.e., for 2MASS 1439+1929 (L1), 2MASS 1507–1627 (L5), and 2MASS 0559–1404 (T4.5). The FeH features are still absent from the models in the early- to mid-type L dwarfs, but overall, very good fits in the J band can be obtained for the whole spectral sequence. Except for 2MASS 1439+1929 (L1) and 2MASS 0036+1821 (L3.5), the T_{eff} values obtained with the J band are consistent with those derived from fitting the full SED.

4.4.3. K Band Fits

Figure 16 shows the spectra and best fitting models over the 1.9 to 2.4 μm wavelength range. The improvement in the quality of the fits is substantial when the K -band spectra are fitted alone. Indeed the agreement between the synthetic spectra and data is at its highest at these wavelengths; the detailed structure of the H₂O, CO, and CH₄ absorption features throughout this wavelength range are almost perfectly reproduced by the models (see Figure 17). However the improvement in the fits comes from a change in T_{eff} of up to 300 K and the K -band T_{eff} values show more scatter. Blake et al. (2007) have fitted high resolution ($R \approx 50000$) 2.296–2.308 μm spectra of nine L dwarfs spanning spectral types L0 to L6 using our model atmospheres and also find good agreement between the data and models.

4.4.4. L Band Fits

Figure 18 shows the spectra and best fitting models over the 3.0 to 4.1 μm wavelength range. There is a marked improvement in the quality of the fits when the L -band spectra are fitted separately. The early- to mid-type L dwarfs no longer show the deep Q-branch CH₄ absorption and the CH₄ band in DENIS 0255–4700 (L8), SDSS J1254–0122 (T2), and 2MASS 0559–1404 (T4.5) is well matched by the synthetic spectra. The model spectrum now fits the peak flux in the spectrum of 2MASS 0559–1404 at 4.1 μm well. The derived T_{eff} values are systematically hotter than those we obtained from the other bands by up to 500 K for all the dwarfs except 2MASS 0559–1404 (Fig. 13) which indicates that the L band is a poor spectral region from which to derive atmospheric parameters of L and T dwarfs. The low value of f_{MC} for some of the dwarfs in our sample (Table 5) reinforces this conclusion.

4.4.5. IRS/SL Fits

Figure 19 shows the data and best fitting models over the 5.5 to 14.5 μm wavelength range. There is also a marked improvement in the fits over this wavelength range since the strengths of the H₂O, CH₄, and NH₃ bands are well reproduced by the model spectra. As first noted by Cushing et al. (2006), there is a mismatch between the data and the models from 9 to 11 μm in the spectra of the mid-type L dwarfs. This mismatch is most prominent in the spectrum of 2MASS 2224–0148 (c.f., Fig. 9, Cushing et al. 2006) but can also be seen weakly in 2MASS 0036+1821 (L3.5) and 2MASS 1507–1627 (L5). Cushing et al. have tentatively identified this feature as arising from the Si-O stretching mode of small silicate grains that give rise to the classic 10 μm silicate feature. Helling et al. (2006) suggest that the absorption feature could arise from quartz (SiO₂) grains, although this is not expected from equilibrium chemistry.

The derived T_{eff} values for the early- to mid-type L dwarfs (Fig. 13) are well above the globally determined values (Fig. 5) by up to 700 K. For four dwarfs, the best fit is found in the high- T_{eff} high- g corner of our model grid ($T_{\text{eff}}=2400$ K, $\log g=5.5$) and should be considered with caution. The IRS/SL spectral range gives T_{eff} values that behave much like those obtained by fitting the L band. Both the L and IRS/SL bands probe regions of the atmosphere with the the lowest pressures and temperatures. The tendency of the L and IRS/SL band fits to produce high T_{eff} values combined with the fact that the

global 0.9–14.5 μm fits tend to over predict the depth of the 3.3 and 7.8 μm methane bands implies that the tops of the model atmospheres may be too cold. This could be simply due to flux redistribution caused by inadequate CH_4 opacities at $\lambda < 1.7 \mu\text{m}$ or a different vertical distribution of opacity within the cloud. On the other hand, atmosphere models also tend to under-predict the temperatures of the middle and upper atmospheres of solar system giant planets (e.g., Marley & McKay 1999), even when accounting for the effects of incident radiation and photochemistry. One possible explanation for this discrepancy is that upwardly propagating waves launched within the convection region break and deposit their energy in the lower pressure regions of the atmosphere (e.g., the discussion in Young et al. (2005) for Jupiter). An exploration of the possible effects of such waves in ultracool dwarf atmospheres would be of interest.

Saumon et al. (2006, 2007) have found that the IRS/SL spectra of Gl 570D (T7.5) and 2MASS J04151954–0935066 (T7) can be modeled adequately only by reducing the abundance of NH_3 by about an order magnitude from that predicted by chemical equilibrium. This is attributed the vertical motions of the gas within the atmospheres which prevents the abundances of N_2 and NH_3 from reaching their expected equilibrium values (Lodders & Fegley 2002). The models presented herein do not include the effects of non-equilibrium chemistry. We note that an equilibrium model fits the IRS/SL spectrum of 2MASS 0559–1404 (T4.5) well. This is a consequence of its higher T_{eff} , which decreases the effect of vertical transport on the chemistry of NH_3 . Nevertheless, a non-equilibrium model provides a better fit to the NH_3 features of the IRS Short High spectrum ($R \approx 600$) of this object at a 2- σ level (Mainzer et al. 2007).

4.4.6. 0.95–2.5 μm Fits

Figure 20 shows the data and best fitting models over the 0.95 to 2.5 μm wavelength range. With the exceptions of 2MASS 1439+1929 (L1) and SDSS 1254–0122 (T2), fitting the near-infrared wavelengths alone does not dramatically improve the quality of the fits. Indeed the same model ([1700/5.5/3]) fits both the near-infrared and 0.95–14.5 μm spectra of 2MASS 0036+1821 (L3.5). Still, the depths of the H_2O and CH_4 bands in the remaining dwarfs are better matched when fitting the near-infrared spectra alone. Note also that the near-infrared spectra of 2MASS 0036+1821 (L3.5) and 2MASS 1507–1627 (L5) are fit by the same model (1700/5.5/f3). The derived T_{eff} values do not match the 0.95–14.5 μm T_{eff} values well, particularly for the early- to mid-type L dwarfs. This implies that spectra at $\lambda \gtrsim 2.5 \mu\text{m}$ are necessary in order to derive T_{eff} values for early- to mid-type L dwarfs. This is unfortunate since most published spectra of L dwarfs rarely extend beyond 2.5 μm .

4.5. The L/T Transition

The transition from the L to T dwarfs is marked by a rapid change in near-infrared color from the very red late-type L dwarfs ($J - K \sim 2.5$) to the very blue T dwarfs ($J - K \sim -1$) and an increase in the emergent flux in the 1 μm region (Dahn et al. 2002; Tinney et al. 2003; Vrba et al. 2004). The latter trend was unexpected because theoretical L_{bol} declines as a brown dwarf

cools. The 0.9896 μm FeH bandhead also strengthens in the spectra of the early- to mid-type T dwarfs after weakening considerably in the spectra of the late-type L dwarfs (Burgasser et al. 2002b; McLean et al. 2003). Furthermore, the transition occurs over a very small T_{eff} range, perhaps only 100 to 200 K (Golimowski et al. 2004). All current atmospheric and evolutionary models (Marley et al. 2002; Tsuji 2005; Burrows et al. 2006) fail to reproduce these observations.

A number of possible solutions have been proposed including the break up of the condensate cloud decks (Ackerman & Marley 2001; Burgasser et al. 2002b), a rapid change in the efficiency of condensate sedimentation (Knapp et al. 2004), or even “crypto-binarity” (Burrows et al. 2006). Unresolved binaries do play a role in exaggerating the magnitude of the 1 μm brightening in the field population (Burgasser et al. 2006b; Burgasser 2007; Liu et al. 2006) but the brightening appears to be intrinsic to the evolution of brown dwarf atmospheres since it has also been observed in binary systems composed of early-type and mid-type T dwarfs. In these systems, whose components presumably have the same metallicity and are coeval, the component with the *later* spectral type is *brighter* in the *J* band (Burgasser et al. 2005; Liu et al. 2006).

Although the models involving changes in the condensate cloud properties are both consistent with the color magnitude diagrams of field L and T dwarfs at the L/T transition (Burgasser et al. 2002b; Knapp et al. 2004), the model spectra have yet to be directly compared to spectroscopic observations. Indeed an error in the TiO line list used in a previous generation of our models (see §3) produced emergent spectra with TiO bands at near-infrared wavelengths that were much too strong, but whose *J*- and *K*-band magnitudes nevertheless matched the colors of L dwarfs relatively well. Unfortunately, self-consistent models that include the break-up of the condensate clouds decks are not yet available so we can only compare models with changes in the sedimentation efficiency f_{sed} .

Four of the dwarfs in our sample span the L/T transition: 2MASS 0825+2115 (L7.5), DENIS 0255–4700 (L8), SDSS J1254–0122 (T2), and 2MASS 0559–1404 (T4.5). As can be seen in Figure 6 and Table 3, the effective temperatures derived from fitting the 0.9–14.5 μm spectra of these four dwarfs decrease slightly from 1400 K to 1200 K and the clouds become gradually thinner (f_{sed} increases) toward later spectral types. Our fits of the SEDs of late-type L and early-type T dwarfs therefore support the concept of a rapid decrease in the overall cloud opacity over a narrow range in T_{eff} .

Burgasser et al. (2002b) argue that the resurgence of the 0.9896 μm FeH bandhead in the spectra of early- to mid-type T dwarfs (see also McLean et al. 2003) is consistent with the cloud breakup hypothesis. In the absence of such a breakup, radiation at $\sim 1 \mu\text{m}$ only emerges from atmospheric layers above the Fe cloud deck in which gaseous FeH has almost completely been depleted into solid or liquid Fe. If holes are present in the cloud decks, radiation from atmospheric layers below the Fe cloud deck where FeH has not been depleted can escape and as a result, the FeH bandhead is observed in the spectra.

Figure 21 shows a sequence of models with $T_{\text{eff}}=1400$ K, $\log g=5.0$, and $f_{\text{sed}}=1, 2, 3, 4$, and nc. The strength of

the FeH bandhead also increases in strength with increasing sedimentation efficiency. For a fixed P/T profile, the FeH column density above the Fe cloud base ($T \sim 2000$ K) is set by the vapor pressure of Fe and thus is independent of both metallicity and f_{sed} ¹⁴. In the $f_{\text{sed}}=1$ model, the $\tau \sim 2/3$ level is high in the cloud ($T \approx 1500$ K) but as f_{sed} increases, the Fe cloud becomes thinner and the $\tau \sim 2/3$ level is reached deeper in the atmosphere. As a result, the column density of FeH that is observed increases resulting in an increase in the band strength of FeH. Therefore a change in sedimentation efficiency at a fixed T_{eff} can also explain the resurgence of the FeH bandhead across the L/T transition.

4.6. Very Red L Dwarfs

As can be seen in Figure 1, there is significant scatter (~ 0.5 – 1 mag) in the near-infrared colors of L and T dwarfs at a given spectral type. It has been suggested that this spread arises from variations in the condensate cloud properties (Knapp et al. 2004) or surface gravity (Burrows et al. 2006), although unresolved binaries also contribute to the scatter (Liu & Leggett 2005). In our models, both surface gravity and cloud sedimentation efficiency affect the near-infrared colors, but the latter dominates for the mid- to late-type L dwarfs. Two pairs of objects in our sample, 2MASS 2224–1058/2MASS 1507–1627 and 2MASS J0825+2115/DENIS J0255–4700, have identical spectral types within the errors but markedly different $J - K_s$ colors: 2.05/1.52 and 2.07/1.69, respectively. As a result, they are ideal for studying the dependence of surface gravity and the condensate cloud properties on the colors of L dwarfs at a given spectral type.

The best fitting model spectra over the 0.95 to 14.5 μm wavelength range for 2MASS 2224–0158 and 2MASS 1507–1627 have [1700/4.5/1] and [1700/4.5/2], respectively. The two objects have the same $\log g$ and T_{eff} values, but the redder object, 2MASS 2224–0158 has an f_{sed} value of 1 while the bluer 2MASS J1507–1627 has $f_{\text{sed}}=2$. Condensate clouds with $f_{\text{sed}}=1$ are thicker and have smaller particles and therefore contribute more opacity to the atmosphere (which result in redder $J - K_s$ colors (see §3)). Burgasser et al. (2007) have also noted that the broad absorption feature seen in the IRS spectrum of 2MASS J2224–0158, which Cushing et al. (2006) have tentatively identified as arising from small silicate grains in the condensate clouds (see §4.4.5), is much weaker in the IRS spectrum of the bluer 2MASS 1507–1627. This is consistent with the condensate clouds being responsible for the very red color of 2MASS 2224–0158.

Similarly, the best fitting model spectra over the 0.95 to 14.5 μm wavelength range for 2MASS 0825+2115 and DENIS 0255–4700 have [1400/4.5/1] and [1400/5.5/2], respectively. These two objects have identical T_{eff} and

¹⁴ The formation of FeH gas can be written as $\text{Fe (gas)} + 0.5 \text{H}_2 = \text{FeH (gas)}$. If Fe is condensed, the partial pressure of Fe (gas) is fixed by the vapor pressure of the iron and is independent of the total amount of condensed phase. Since the partial pressure of H_2 is essentially a constant (at a given total pressure), the partial pressure of FeH is also fixed. Therefore once Fe condenses, the partial pressure, and thus column density, of FeH above the Fe cloud base is independent of both metallicity and f_{sed} for a fixed P/T profile.

different $\log g$ values but as above, the redder object, 2MASS 0825+2115, has $f_{\text{sed}}=1$. These latter two objects show how both surface gravity and the condensate clouds play a role in controlling the colors of L dwarfs.

5. SYSTEMATIC UNCERTAINTIES

Both the G statistic and the Monte Carlo simulations used in this analysis explicitly account for the random errors in the data. However it is important to also understand any systematic errors that can affect the analysis. Below, we discuss two such systematic errors, the absolute flux calibration process and the choice of the weights in the G statistic.

5.1. Absolute Flux Calibration

The near-infrared spectra used in this work were obtained with SpeX on the NASA IRTF. The 0.8–2.5 μm wavelength range is covered in six cross-dispersed orders, and as a result the spectra from the various orders are merged into a single spectrum by scaling the spectra to ensure that the flux density levels match in regions where the spectra overlap in wavelength. Unfortunately there is no wavelength overlap between the H and K bands and therefore no scaling could be performed. The merged 0.8–2.5 μm spectra were then absolutely flux calibrated by deriving a *single* scale factor based on the 2MASS JHK_s photometry. Cushing et al. (2005) showed that, on average, the synthetic colors ($J - H$, $H - K_s$, and $J - K_s$) of their entire sample of M, L, and T dwarfs match the observed 2MASS colors within the errors. However in some cases, we find deviations between the synthetic and observed colors of up to 2σ .

In order to quantify any effect that variations in the absolute flux calibration of the near-infrared spectra have on our analysis, we have absolutely flux calibrated each of the SpeX cross-dispersed spectra separately using both 2MASS photometry and Mauna Kea Observatories Near-Infrared (MKO-NIR; Tokunaga et al. 2002) photometry (Knapp et al. 2004)¹⁵. Two of the dwarfs in our sample, 2MASS 1506+1321 and DENIS J0255–4700, have not been observed in the MKO-NIR system to date. The near-infrared, L band, and IRS/SL spectra are then recombined into a single 0.95–14.5 μm spectrum and the entire analysis is performed again.

Figure 22 summarizes the differences between the atmospheric parameters derived by fitting the spectra with the different absolute flux calibration schemes over the 0.95–14.5 μm wavelength range. Flux calibrating the spectra with 2MASS photometry leaves the derived parameters almost unchanged while the derived parameters for three objects flux calibrated with the MKO-NIR photometry change by 100 K in T_{eff} and 0.5 dex in $\log g$. Overall, there is little change in the derived values of T_{eff} , $\log g$, and f_{sed} which indicates the absolute flux calibration does not severely affect the parameters derived by fitting the 0.95–14.5 μm spectra (Figure 23). The parameters obtained by fitting the 0.95–2.5 μm spectra alone are more sensitive to variations in the absolute flux calibration. Differences of 0.5–1 dex in $\log g$, 100 K in

¹⁵ The 2MASS J band filter spans two spectral orders and therefore we have scaled these two orders to the same flux density levels by eye. The two orders are then absolutely flux calibrated together using J -band photometry.

T_{eff} , and 1 in f_{sed} in the best fitting model spectra are apparent. The range of possible models (i.e., the error bars) also grows because the SpeX cross-dispersed orders (J , H , K) are absolutely flux calibrated separately and thus are varied separately in the Monte Carlo simulation.

5.2. Weights

As discussed in §4.1, we weight each pixel in the spectrum by its width ($w_i = \Delta\lambda_i$) to remove a bias introduced into the G statistic due to the large variation in wavelength sampling of the data. Our choice of weights, however, is completely arbitrary. In order to estimate any systematic error in the derived parameters introduced by our choice of weighting scheme, we have devised a second weighting scheme as follows.

We divide the 0.95–14.5 μm wavelength range into bins equally-spaced in $\ln\lambda$. Each pixel that falls in bin k receives a weight inversely proportional to the total number of pixels contained in bin k . For example, if bin k contains four pixels, then $w_i=0.25$ for each pixel in bin k . The *Spitzer* data has the lowest resolving power of all the data ($R \equiv \lambda/\Delta\lambda \approx 100$) so we used a bin size of $\delta \ln \lambda = 0.01$ which corresponds to $R=100$. This alternative weighting scheme effectively mimics smoothing the spectra to $R=100$ and resampling them such that each pixel corresponds to a single resolution element.

Figure 24 summarizes the differences between the atmospheric parameters derived by fitting the data using the two different weight schemes over the 0.95–14.5 μm wavelength range. The T_{eff} values derived for the early-type L dwarfs are lower by 100 K and the derived $\log g$ values for two of the dwarfs change by 1 and 0.5. Based on these results, the choice of weighting scheme does not dramatically alter the results presented herein.

6. CONCLUSIONS

We have performed the first fits of the 0.95–14.5 μm SEDs of nine field ultracool dwarfs spanning spectral types L1 to T4.5 to obtain effective temperatures, gravities and values for the cloud sedimentation parameter. The wide wavelength coverage of the data allows us to easily discriminate between synthetic spectra with different atmospheric parameters because most physical and chemical processes that occur in ultracool dwarf atmospheres leave a signature in one or more of the wavelength regions covered by the data.

In our study of field ultracool dwarfs we have focused on the most significant physical parameters, ignoring the more subtle effects of metallicity variations from the solar value as well as departures from chemical equilibrium caused by vertical mixing in the atmosphere (e.g. Saumon et al. (2006)). The spectroscopic data come from a variety of instruments and we have estimated the uncertainties in the derived parameters that arise from the absolute flux calibrations of the various spectra that form the SEDs. Although some wavelength ranges are poorly fitted for some objects, undoubtedly due to remaining inadequacies in the models and, to a smaller extent, to possible variations in metallicity amongst the dwarfs in our sample, overall the model spectra fit the data well.

Given the natural scatter in the observational properties among the objects in our sample and the uncertainties inherent in our procedure, we can identify only gen-

eral trends in the fitted parameters as a function of spectral type. The effective temperatures decrease steadily through the L1 to T4.5 spectral types and agree with the determinations of Golimowski et al. (2004). Our results also confirm that T_{eff} is nearly constant at the L/T transition, decreasing by only ~ 200 K from spectral types L7.5 to T4.5.

Two topics of great interest are the evolution of the cloud properties as a function of spectral type and the distribution of cloud properties within each spectral subclass. Our work provides a first, although somewhat blurry glimpse of this important aspect of ultracool dwarf atmospheres. We find that the cloud properties, as encapsulated in the most important free parameter of the Ackerman & Marley (2001) condensation cloud model, f_{sed} , vary significantly among L dwarfs, ranging from very thick clouds ($f_{\text{sed}} = 1$) to relatively thin clouds ($f_{\text{sed}} = 3$) with no particular trend with spectral type. The two L dwarfs in our sample with very red near-infrared colors have best fitting model spectra with thick clouds. Finally the fits to the two T dwarfs in our sample (T2 and T4.5) suggest that the clouds becomes thinner in this spectral class, in agreement with previous studies.

Fitting individual spectral bands, we almost always obtain excellent fits to the data, in some cases down to the fine structure of the H_2O and CH_4 bands. The T_{eff} obtained in this fashion (Fig. 13) can show quite a bit of scatter compared to the values derived by fitting the full SED, typically by ~ 200 K and in the worst cases, up to 700 K. Nevertheless, the trend of decreasing T_{eff} with spectral type is preserved in all bands, with few exceptions. However, this exercise shows that in general, T_{eff} determinations based on the analysis of narrow spectral ranges are not reliable for ultracool dwarfs.

The data point to several directions for improving the models. First, improved input molecular opacities, particularly for CrH, VO, FeH, and CH_4 and the resonance doublet of K I (7665, 7699 \AA) (Allard et al. 2007) are required to improve fits to the early L and all of the T dwarfs, respectively. The second important area ripe for improvement remains the cloud model, in particular the particles' size distribution, the cloud's vertical profile, and the optical properties of the condensates.

The accurate determination of the physical parameters of isolated field ultracool dwarfs therefore remains an elusive goal. Our method of SED fitting should be applied to those ultracool dwarfs with well constrained T_{eff} (± 20 K) and $\log g$ (± 0.05 dex) values (derived from other methods) in order to better assess its internal uncertainties. Currently, such a sample is limited to a few late-type T dwarfs (Saumon et al. 2006, 2007; Liu et al. 2007) that are companions to main sequence stars with known distances, metallicities and well-constrained ages. Such studies should be extended to include earlier spectral types in order to firmly associate the observable properties of the L and T spectral sequence to fundamental astrophysical parameters.

We thank Adam Burgasser and Kelle Cruz for useful discussions, Mike Liu for suggestions that improved the original manuscript, and the anonymous referee for his/her careful review of the manuscript and constructive comments. This publication makes use of data

from the Two Micron All Sky Survey, which is a joint project of the University of Massachusetts and the Infrared Processing and Analysis Center, and funded by the National Aeronautics and Space Administration and the National Science Foundation, the SIMBAD database, operated at CDS, Strasbourg, France, NASA's Astrophysics Data System Bibliographic Services, the M, L, and T dwarf compendium housed at DwarfArchives.org and maintained by Chris Gelino, Davy Kirkpatrick, and Adam Burgasser, and the NASA/ IPAC Infrared Science Archive, which is operated by the Jet Propulsion Laboratory, California Institute of Technology, under contract with the National Aeronautics and Space Administration. This work is based (in part) on observations made with the *Spitzer Space Telescope*, which is operated by the Jet Propulsion Laboratory, California Institute of Technology under a contract with NASA and is supported (in part) by the United States Department of Energy under contract W-7405-ENG-36, NASA through the Spitzer Space Telescope Fellowship Program, through a contract issued by the Jet Propulsion Laboratory, California Institute of Technology under a contract with NASA. Work by K.L. is supported by NSF grant AST0406963, NASA grant NNG06GC26G, and the NASA Office of Space Science. M.S.M acknowledges support from the NASA Office of Space Science.

Facilities: Keck (LRIS), IRTF (SpeX), Subaru (IRCS), Spitzer (IRS).

REFERENCES

- Ackerman, A. S. & Marley, M. S. 2001, *ApJ*, 556, 872
- Allard, F., Allard, N. F., Homeier, D., Kielkopf, J., McCaughrean, M. J., & Spiegelman, F. 2007, *A&A*, 474, L21
- Allard, F. & Hauschildt, P. H. 1995, *ApJ*, 445, 433
- Allard, F., Hauschildt, P. H., Alexander, D. R., & Starrfield, S. 1997, *ARA&A*, 35, 137
- Allard, F., Hauschildt, P. H., Baraffe, I., & Chabrier, G. 1996, *ApJ*, 465, L123+
- Allen, P. R., Koerner, D. W., Reid, I. N., & Trilling, D. E. 2005, *ApJ*, 625, 385
- Baraffe, I., Chabrier, G., Allard, F., & Hauschildt, P. H. 1997, *A&A*, 327, 1054
- Basri, G., Mohanty, S., Allard, F., Hauschildt, P. H., Delfosse, X., Martín, E. L., Forveille, T., & Goldman, B. 2000, *ApJ*, 538, 363
- Blake, C. H., Charbonneau, D., White, R. J., Marley, M. S., & Saumon, D. 2007, *ApJ*, 666, 1198
- Borysow, A., Jorgensen, U. G., & Zheng, C. 1997, *A&A*, 324, 185
- Burgasser, A. J. 2007, *ApJ*, 659, 655
- Burgasser, A. J., Geballe, T. R., Leggett, S. K., Kirkpatrick, J. D., & Golimowski, D. A. 2006a, *ApJ*, 637, 1067
- Burgasser, A. J., Kirkpatrick, J. D., Brown, M. E., Reid, I. N., Burrows, A., Liebert, J., Matthews, K., Gizis, J. E., Dahn, C. C., Monet, D. G., Cutri, R. M., & Skrutskie, M. F. 2002a, *ApJ*, 564, 421
- Burgasser, A. J., Kirkpatrick, J. D., Cruz, K. L., Reid, I. N., Leggett, S. K., Liebert, J., Burrows, A., & Brown, M. E. 2006b, *ApJS*, 166, 585
- Burgasser, A. J., Kirkpatrick, J. D., Liebert, J., & Burrows, A. 2003a, *ApJ*, 594, 510
- Burgasser, A. J., Kirkpatrick, J. D., Reid, I. N., Brown, M. E., Miskay, C. L., & Gizis, J. E. 2003b, *ApJ*, 586, 512
- Burgasser, A. J.,Looper, D. L., Kirkpatrick, J. D., Cruz, K. L., & Swift, B. 2007, *apJ*, in press (astro 0710.1123)
- Burgasser, A. J., Marley, M. S., Ackerman, A. S., Saumon, D., Lodders, K., Dahn, C. C., Harris, H. C., & Kirkpatrick, J. D. 2002b, *ApJ*, 571, L151
- Burgasser, A. J., Reid, I. N., Leggett, S. K., Kirkpatrick, J. D., Liebert, J., & Burrows, A. 2005, *ApJ*, 634, L177
- Burrows, A., Hubbard, W. B., Lunine, J. I., & Liebert, J. 2001, *Reviews of Modern Physics*, 73, 719
- Burrows, A., Marley, M., Hubbard, W. B., Lunine, J. I., Guillot, T., Saumon, D., Freedman, R., Sudarsky, D., & Sharp, C. 1997, *ApJ*, 491, 856
- Burrows, A. & Sharp, C. M. 1999, *ApJ*, 512, 843
- Burrows, A., Sudarsky, D., & Hubeny, I. 2006, *ApJ*, 640, 1063
- Burrows, A. & Volobuyev, M. 2003, *ApJ*, 583, 985
- Cheung, A. S.-C., Taylor, A. W., & Merer, A. J. 1982, *Journal of Molecular Spectroscopy*, 92, 391
- Costa, E., Méndez, R. A., Jao, W.-C., Henry, T. J., Subasavage, J. P., & Ianna, P. A. 2006, *AJ*, 132, 1234
- Cruz, K. L., Reid, I. N., Liebert, J., Kirkpatrick, J. D., & Lowrance, P. J. 2003, *AJ*, 126, 2421
- Cushing, M. C., Rayner, J. T., Davis, S. P., & Vacca, W. D. 2003, *ApJ*, 582, 1066
- Cushing, M. C., Rayner, J. T., & Vacca, W. D. 2005, *ApJ*, 623, 1115
- Cushing, M. C., Roellig, T. L., Marley, M. S., Saumon, D., Leggett, S. K., Kirkpatrick, J. D., Wilson, J. C., Sloan, G. C., Mainzer, A. K., Van Cleve, J. E., & Houck, J. R. 2006, *ApJ*, 648, 614
- Dahn, C. C., Harris, H. C., Vrba, F. J., Guetter, H. H., Canzian, B., Henden, A. A., Levine, S. E., Luginbuhl, C. B., Monet, A. K. B., Monet, D. G., Pier, J. R., Stone, R. C., Walker, R. L., Burgasser, A. J., Gizis, J. E., Kirkpatrick, J. D., Liebert, J., & Reid, I. N. 2002, *AJ*, 124, 1170
- Dulick, M., Bauschlicher, C. W., Burrows, A., Sharp, C. M., Ram, R. S., & Bernath, P. 2003, *ApJ*, 594, 651
- Epchtein, N., de Batz, B., Capoani, L., Chevallier, L., Copet, E., Fouque, P., Lacombe, F., Le Bertre, T., Pau, S., Rouan, D., Ruphy, S., Simon, G., Tiphene, D., Burton, W. B., Bertin, E., Deul, E., Habing, H., Borsenberger, J., Dennefeld, M., Guglielmo, F., Loup, C., Mamon, G., Ng, Y., Omont, A., Provost, L., Renault, J.-C., Tanguy, F., Kimeswenger, S., Kienel, C., Garzon, F., Persi, P., Ferrari-Toniolo, M., Robin, A., Paturel, G., Vauglin, I., Forveille, T., Delfosse, X., Hron, J., Schultheis, M., Appenzeller, I., Wagner, S., Balazs, L., Holl, A., Lepine, J., Boscolo, P., Picazzo, E., Duc, P.-A., & Mennessier, M.-O. 1997, *The Messenger*, 87, 27
- Fegley, B. J. & Lodders, K. 1994, *Icarus*, 110, 117
- 1996, *ApJ*, 472, L37
- Fortney, J. J., Marley, M. S., Lodders, K., Saumon, D., & Freedman, R. 2005, *ApJ*, 627, L69
- Fortney, J. J., Saumon, D., Marley, M. S., Lodders, K., & Freedman, R. S. 2006, *ApJ*, 642, 495
- Freedman, R. S., Marley, M. S., & Lodders, K. 2007, submitted
- Galehouse, D. C., Davis, S. P., & Brault, J. W. 1980, *ApJS*, 42, 241
- Geballe, T. R., Knapp, G. R., Leggett, S. K., Fan, X., Golimowski, D. A., Anderson, S., Brinkmann, J., Csabai, I., Gunn, J. E., Hawley, S. L., Hennessy, G., Henry, T. J., Hill, G. J., Hindsley, R. B., Ivezić, Z., Lupton, R. H., McDaniel, A., Munn, J. A., Narayanan, V. K., Peng, E., Pier, J. R., Rockosi, C. M., Schneider, D. P., Smith, J. A., Strauss, M. A., Tsvetanov, Z. I., Uomoto, A., York, D. G., & Zheng, W. 2002, *ApJ*, 564, 466
- Geballe, T. R., Saumon, D., Leggett, S. K., Knapp, G. R., Marley, M. S., & Lodders, K. 2001, *ApJ*, 556, 373
- Gizis, J. E., Monet, D. G., Reid, I. N., Kirkpatrick, J. D., Liebert, J., & Williams, R. J. 2000, *AJ*, 120, 1085
- Golimowski, D. A., Leggett, S. K., Marley, M. S., Fan, X., Geballe, T. R., Knapp, G. R., Vrba, F. J., Henden, A. A., Luginbuhl, C. B., Guetter, H. H., Munn, J. A., Canzian, B., Zheng, W., Tsvetanov, Z. I., Chiu, K., Glazebrook, K., Hoversten, E. A., Schneider, D. P., & Brinkmann, J. 2004, *AJ*, 127, 3516
- Goody, R., West, R., Chen, L., & Crisp, D. 1989, *Journal of Quantitative Spectroscopy and Radiative Transfer*, 43, 191
- Helling, C., Klein, R., Woitke, P., Nowak, U., & Sedlmayr, E. 2004, *A&A*, 423, 657
- Helling, C., Oevermann, M., Lüttke, M. J. H., Klein, R., & Sedlmayr, E. 2001, *A&A*, 376, 194
- Helling, C., Thi, W.-F., Woitke, P., & Fridlund, M. 2006, *A&A*, 451, L9
- Helling, C. & Woitke, P. 2006, *A&A*, 455, 325
- Hillenbrand, L. A., Foster, J. B., Persson, S. E., & Matthews, K. 2002, *PASP*, 114, 708
- Houck, J. R., Roellig, T. L., van Cleve, J., Forrest, W. J., Herter, T., Lawrence, C. R., Matthews, K., Reitsema, H. J., Soifer, B. T., Watson, D. M., Weedman, D., Huisjen, M., Troeltzsch, J., Barry, D. J., Bernard-Salas, J., Blacken, C. E., Brandl, B. R., Charmandaris, V., Devost, D., Gull, G. E., Hall, P., Henderson, C. P., Higdon, S. J. U., Pirger, B. E., Schoenwald, J., Sloan, G. C., Uchida, K. I., Appleton, P. N., Armus, L., Burgdorf, M. J., Fajardo-Acosta, S. B., Grillmair, C. J., Ingalls, J. G., Morris, P. W., & Teplitz, H. I. 2004, *ApJS*, 154, 18
- Kendall, T. R., Jones, H. R. A., Pinfield, D. J., Pokorny, R. S., Folkes, S., Weights, D., Jenkins, J. S., & Mauron, N. 2006, *MNRAS*, 1334
- Kirkpatrick, J. D., Reid, I. N., Liebert, J., Cutri, R. M., Nelson, B., Beichman, C. A., Dahn, C. C., Monet, D. G., Gizis, J. E., & Skrutskie, M. F. 1999, *ApJ*, 519, 802
- Kirkpatrick, J. D., Reid, I. N., Liebert, J., Gizis, J. E., Burgasser, A. J., Monet, D. G., Dahn, C. C., Nelson, B., & Williams, R. J. 2000, *AJ*, 120, 447
- Knapp, G. R., Leggett, S. K., Fan, X., Marley, M. S., Geballe, T. R., Golimowski, D. A., Finkbeiner, D., Gunn, J. E., Hennawi, J., Ivezić, Z., Lupton, R. H., Schlegel, D. J., Strauss, M. A., Tsvetanov, Z. I., Chiu, K., Hoversten, E. A., Glazebrook, K., Zheng, W., Hendrickson, M., Williams, C. C., Uomoto, A., Vrba, F. J., Henden, A. A., Luginbuhl, C. B., Guetter, H. H., Munn, J. A., Canzian, B., Schneider, D. P., & Brinkmann, J. 2004, *AJ*, 127, 3553

- Kobayashi, N., Tokunaga, A. T., Terada, H., Goto, M., Weber, M., Potter, R., Onaka, P. M., Ching, G. K., Young, T. T., Fletcher, K., Neil, D., Robertson, L., Cook, D., Imanishi, M., & Warren, D. W. 2000, in *Proc. SPIE Vol. 4008*, p. 1056-1066, *Optical and IR Telescope Instrumentation and Detectors*, Masanori Iye; Alan F. Moorwood; Eds., 1056-1066
- Leggett, S. K., Saumon, D., Marley, M. S., Geballe, T. R., Golimowski, D. A., Stephens, D., & Fan, X. 2007, *ApJ*, 655, 1079
- Liu, M. C. & Leggett, S. K. 2005, *ApJ*, 634, 616
- Liu, M. C., Leggett, S. K., & Chiu, K. 2007, *ApJ*, 660, 1507
- Liu, M. C., Leggett, S. K., Golimowski, D. A., Chiu, K., Fan, X., Geballe, T. R., Schneider, D. P., & Brinkmann, J. 2006, *ApJ*, 647, 1393
- Lodders, K. 1999, *ApJ*, 519, 793
— 2002, *ApJ*, 577, 974
— 2003, *ApJ*, 591, 1220
- Lodders, K. & Fegley, B. 2002, *Icarus*, 155, 393
- Mainzer, A. K., Roellig, T. L., Saumon, D., Marley, M. S., Cushing, M. C., Sloan, G. C., Kirkpatrick, J. D., Leggett, S. K., & Wilson, J. C. 2007, *ApJ*, 662, 1245
- Marley, M. S. & McKay, C. P. 1999, *Icarus*, 138, 268
- Marley, M. S., Saumon, D., Guillot, T., Freedman, R. S., Hubbard, W. B., Burrows, A., & Lunine, J. I. 1996, *Science*, 272, 1919
- Marley, M. S., Seager, S., Saumon, D., Lodders, K., Ackerman, A. S., Freedman, R. S., & Fan, X. 2002, *ApJ*, 568, 335
- McGovern, M. R., Kirkpatrick, J. D., McLean, I. S., Burgasser, A. J., Prato, L., & Lowrance, P. J. 2004, *ApJ*, 600, 1020
- McKay, C. P., Pollack, J. B., & Courtin, R. 1989, *Icarus*, 80, 23
- McLean, I. S., McGovern, M. R., Burgasser, A. J., Kirkpatrick, J. D., Prato, L., & Kim, S. S. 2003, *ApJ*, 596, 561
- Metchev, S. A. & Hillenbrand, L. A. 2006, *ApJ*, 651, 1166
- Nakajima, T., Oppenheimer, B. R., Kulkarni, S. R., Golimowski, D. A., Matthews, K., & Durrance, S. T. 1995, *Nature*, 378, 463
- Neuhäuser, R., Guenther, E. W., Wuchterl, G., Mugrauer, M., Bedalov, A., & Hauschildt, P. H. 2005, *A&A*, 435, L13
- Oke, J. B., Cohen, J. G., Carr, M., Cromer, J., Dingizian, A., Harris, F. H., Labrecque, S., Lucinio, R., Schaal, W., Epps, H., & Miller, J. 1995, *PASP*, 107, 375
- Rayner, J. T., Toomey, D. W., Onaka, P. M., Denault, A. J., Stahlberger, W. E., Vacca, W. D., Cushing, M. C., & Wang, S. 2003, *PASP*, 115, 362
- Reid, I. N., Kirkpatrick, J. D., Gizis, J. E., Dahn, C. C., Monet, D. G., Williams, R. J., Liebert, J., & Burgasser, A. J. 2000, *AJ*, 119, 369
- Reiners, A. & Basri, G. 2006, *ApJ*, 644, 497
- Saumon, D., Geballe, T. R., Leggett, S. K., Marley, M. S., Freedman, R. S., Lodders, K., Fegley, B., & Sengupta, S. K. 2000, *ApJ*, 541, 374
- Saumon, D., Marley, M. S., Cushing, M. C., Leggett, S. K., Roellig, T. L., Lodders, K., & Freedman, R. S. 2006, *ApJ*, 647, 552
- Saumon, D., Marley, M. S., Leggett, S. K., Geballe, T. R., Stephens, D., Golimowski, D. A., Cushing, M. C., Fan, X., Rayner, J. T., Lodders, K., & Freedman, R. S. 2007, *ApJ*, 656, 1136
- Schwenke, D. W. 1998, in *Chemistry and Physics of Molecules and Grains in Space. Faraday Discussions No. 109*, 321
- Skrutskie, M. F., Cutri, R. M., Stiening, R., Weinberg, M. D., Schneider, S., Carpenter, J. M., Beichman, C., Capps, R., Chester, T., Elias, J., Huchra, J., Liebert, J., Lonsdale, C., Monet, D. G., Price, S., Seitzer, P., Jarrett, T., Kirkpatrick, J. D., Gizis, J. E., Howard, E., Evans, T., Fowler, J., Fullmer, L., Hurt, R., Light, R., Kopan, E. L., Marsh, K. A., McCallon, H. L., Tam, R., Van Dyk, S., & Wheelock, S. 2006, *AJ*, 131, 1163
- Takeda, Y. 1995, *PASJ*, 47, 287
- Tinney, C. G., Burgasser, A. J., & Kirkpatrick, J. D. 2003, *AJ*, 126, 975
- Tokunaga, A. T., Simons, D. A., & Vacca, W. D. 2002, *PASP*, 114, 180
- Toon, O. B., McKay, C. P., Ackerman, T. P., & Santhanam, K. 1989, *J. Geophys. Res.*, 94, 16287
- Tsuji, T. 2002, *ApJ*, 575, 264
— 2005, *ApJ*, 621, 1033
- Tsuji, T., Ohnaka, K., Aoki, W., & Nakajima, T. 1996, *A&A*, 308, L29
- Vrba, F. J., Henden, A. A., Luginbuhl, C. B., Guetter, H. H., Munn, J. A., Canzian, B., Burgasser, A. J., Kirkpatrick, J. D., Fan, X., Geballe, T. R., Golimowski, D. A., Knapp, G. R., Leggett, S. K., Schneider, D. P., & Brinkmann, J. 2004, *AJ*, 127, 2948
- Wallace, L. & Hinkle, K. 2001, *ApJ*, 559, 424
- Werner, M. W., Roellig, T. L., Low, F. J., Rieke, G. H., Rieke, M., Hoffmann, W. F., Young, E., Houck, J. R., Brandl, B., Fazio, G. G., Hora, J. L., Gehrz, R. D., Helou, G., Soifer, B. T., Stauffer, J., Keene, J., Eisenhardt, P., Gallagher, D., Gautier, T. N., Irace, W., Lawrence, C. R., Simmons, L., Van Cleve, J. E., Jura, M., Wright, E. L., & Cruikshank, D. P. 2004, *ApJS*, 154, 1
- Woitke, P. & Helling, C. 2003, *A&A*, 399, 297
— 2004, *A&A*, 414, 335
- York, D. G., Adelman, J., Anderson, J. E., Anderson, S. F., Annis, J., Bahcall, N. A., Bakken, J. A., Barkhouser, R., Bastian, S., Berman, E., Boroski, W. N., Bracker, S., Briegel, C., Briggs, J. W., Brinkmann, J., Brunner, R., Burles, S., Carr, L., Carr, M. A., Castander, F. J., Chen, B., Colestock, P. L., Connolly, A. J., Crocker, J. H., Csabai, I., Czarapata, P. C., Davis, J. E., Doi, M., Dombek, T., Eisenstein, D., Ellman, N., Elms, B. R., Evans, M. L., Fan, X., Federwitz, G. R., Fiscelli, L., Friedman, S., Frieman, J. A., Fukugita, M., Gillespie, B., Gunn, J. E., Gurbani, V. K., de Haas, E., Haldeman, M., Harris, F. H., Hayes, J., Heckman, T. M., Hennessy, G. S., Hindsley, R. B., Holm, S., Holmgren, D. J., Huang, C., Hull, C., Husby, D., Ichikawa, S., Ichikawa, T., Ivezić, Z., Kent, S., Kim, R. S. J., Kinney, E., Klaene, M., Kleinman, A. N., Kleinman, S., Knapp, G. R., Korienek, J., Kron, R. G., Kunszt, P. Z., Lamb, D. Q., Lee, B., Leger, R. F., Limmongkol, S., Lindenmeyer, C., Long, D. C., Loomis, C., Loveday, J., Lucinio, R., Lupton, R. H., MacKinnon, B., Mannery, E. J., Mantsch, P. M., Margon, B., McGehee, P., McKay, T. A., Meiksin, A., Merelli, A., Monet, D. G., Munn, J. A., Narayanan, V. K., Nash, T., Neilsen, E., Neswold, R., Newberg, H. J., Nichol, R. C., Nicinski, T., Nonino, M., Okada, N., Okamura, S., Ostriker, J. P., Owen, R., Pauls, A. G., Peoples, J., Peterson, R. L., Petravick, D., Pier, J. R., Pope, A., Pordes, R., Prosapio, A., Rechenmacher, R., Quinn, T. R., Richards, G. T., Richmond, M. W., Rivetta, C. H., Rockosi, C. M., Ruthmansdorfer, K., Sandford, D., Schlegel, D. J., Schneider, D. P., Sekiguchi, M., Sergey, G., Shimasaku, K., Siegmund, W. A., Smee, S., Smith, J. A., Snedden, S., Stone, R., Stoughton, C., Strauss, M. A., Stubbs, C., SubbaRao, M., Szalay, A. S., Szapudi, I., Szokoly, G. P., Thakar, A. R., Tremonti, C., Tucker, D. L., Uomoto, A., Vanden Berk, D., Vogeley, M. S., Waddell, P., Wang, S., Watanabe, M., Weinberg, D. H., Yanny, B., & Yasuda, N. 2000, *AJ*, 120, 1579
- Young, L. A., Yelle, R. V., Young, R., Seiff, A., & Kirk, D. B. 2005, *Icarus*, 173, 185

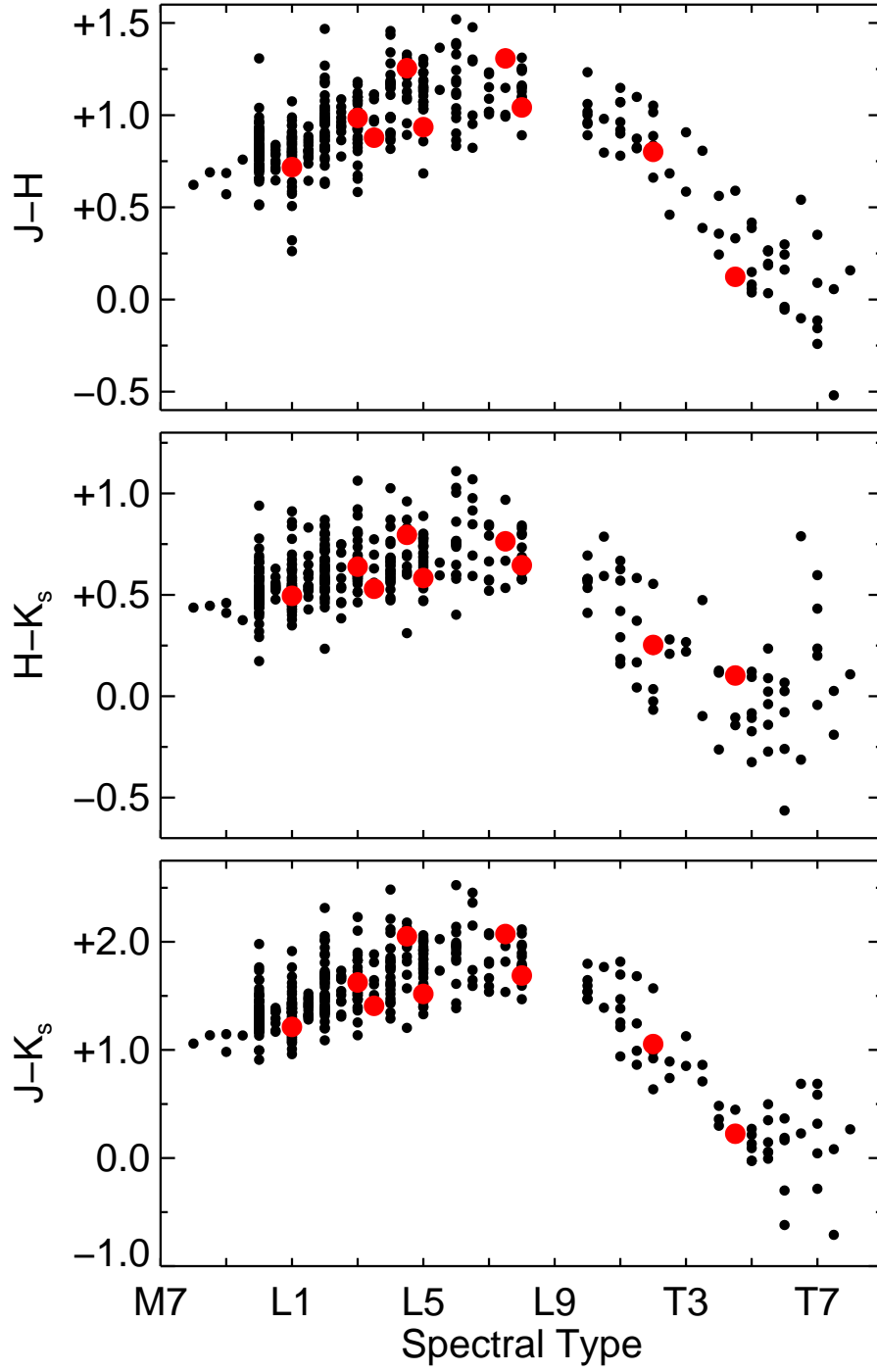


FIG. 1.— 2MASS $J - H$ (top), $H - K_s$ (middle), and $J - K_s$ (bottom) colors as a function of spectral type for all of the L and T dwarfs in the DwarfArchives web site as of 2007-06-07. The dwarfs in our sample are shown in red.

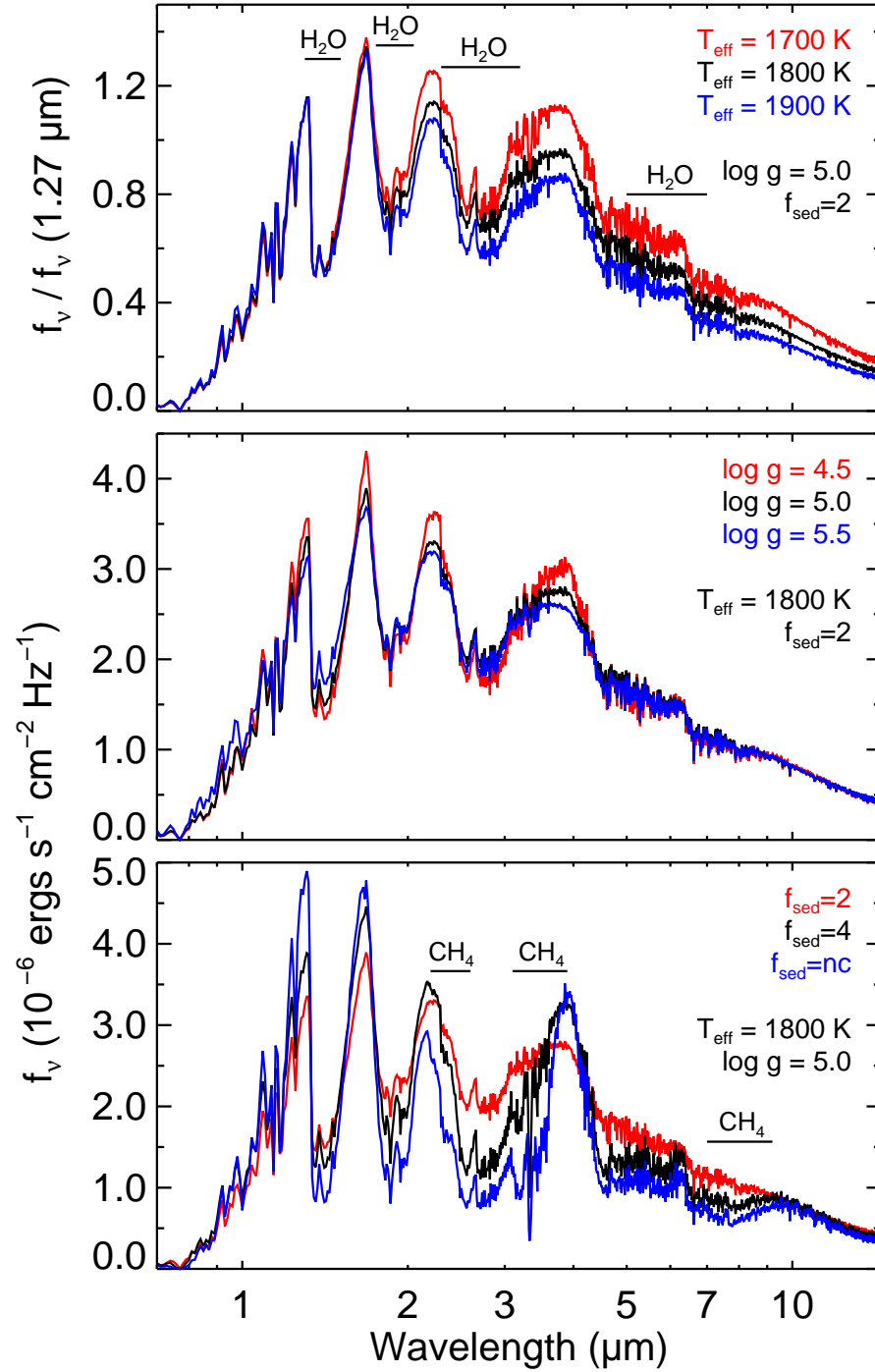


FIG. 2.— A comparison of synthetic spectra with atmospheric parameters typical of an L dwarf ($T_{\text{eff}}=1800 \text{ K}$, $\log g=5.0 \text{ cm s}^{-2}$, $f_{\text{sed}}=2$) when T_{eff} , $\log g$, and f_{sed} are varied. The models have been smoothed to $R=500$ and normalized to unity at $1.27 \mu\text{m}$ in the top panel to show the relative variations in the models as a function of T_{eff} . The flux density units of the models in the lower two panels correspond to the emergent flux at the top of the atmosphere.

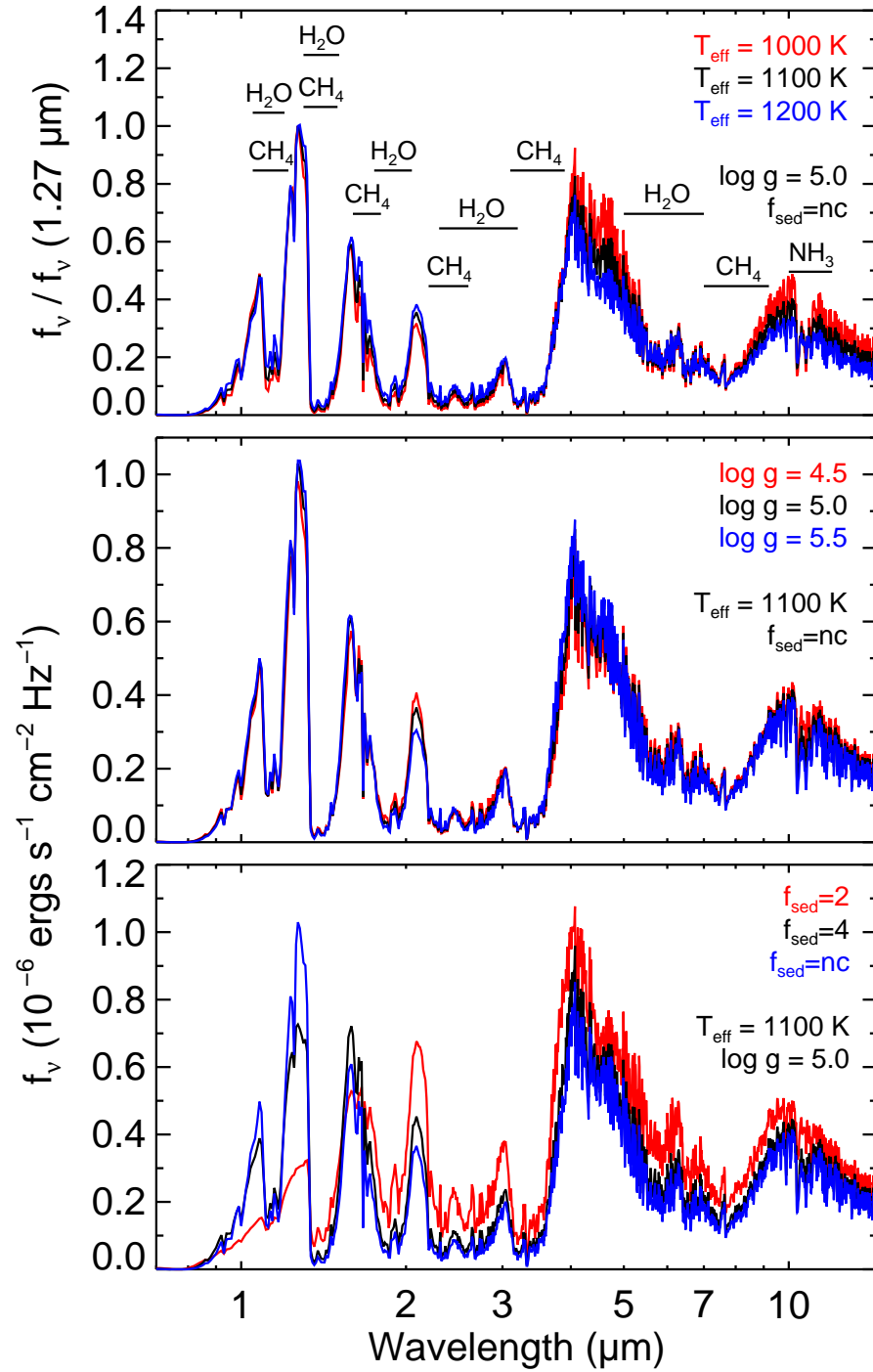


FIG. 3.— Same as Figure 2 except for the atmospheric parameters of a typical T dwarf ($T_{\text{eff}}=1100 \text{ K}$, $\log g=5.0 \text{ cm s}^{-2}$, $f_{\text{sed}}=\text{nc}$).

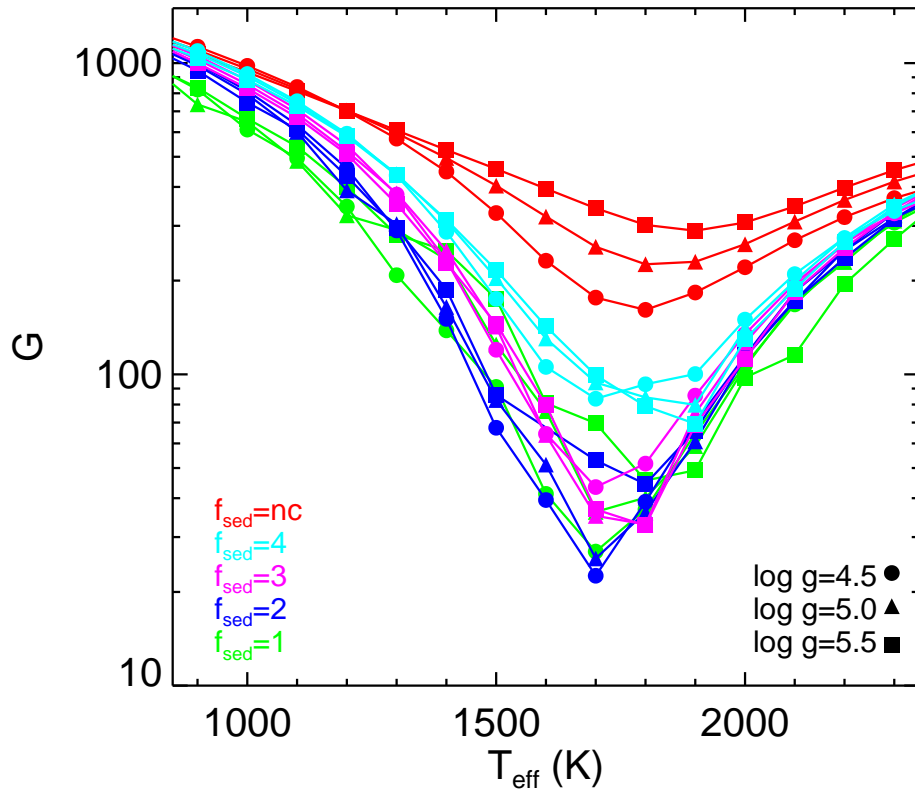


FIG. 4.— The G values as a function of T_{eff} for the 0.95–14.5 μm spectrum of 2MASS 1507–1627 (L5). There is a clear minimum in G at 1700 K.

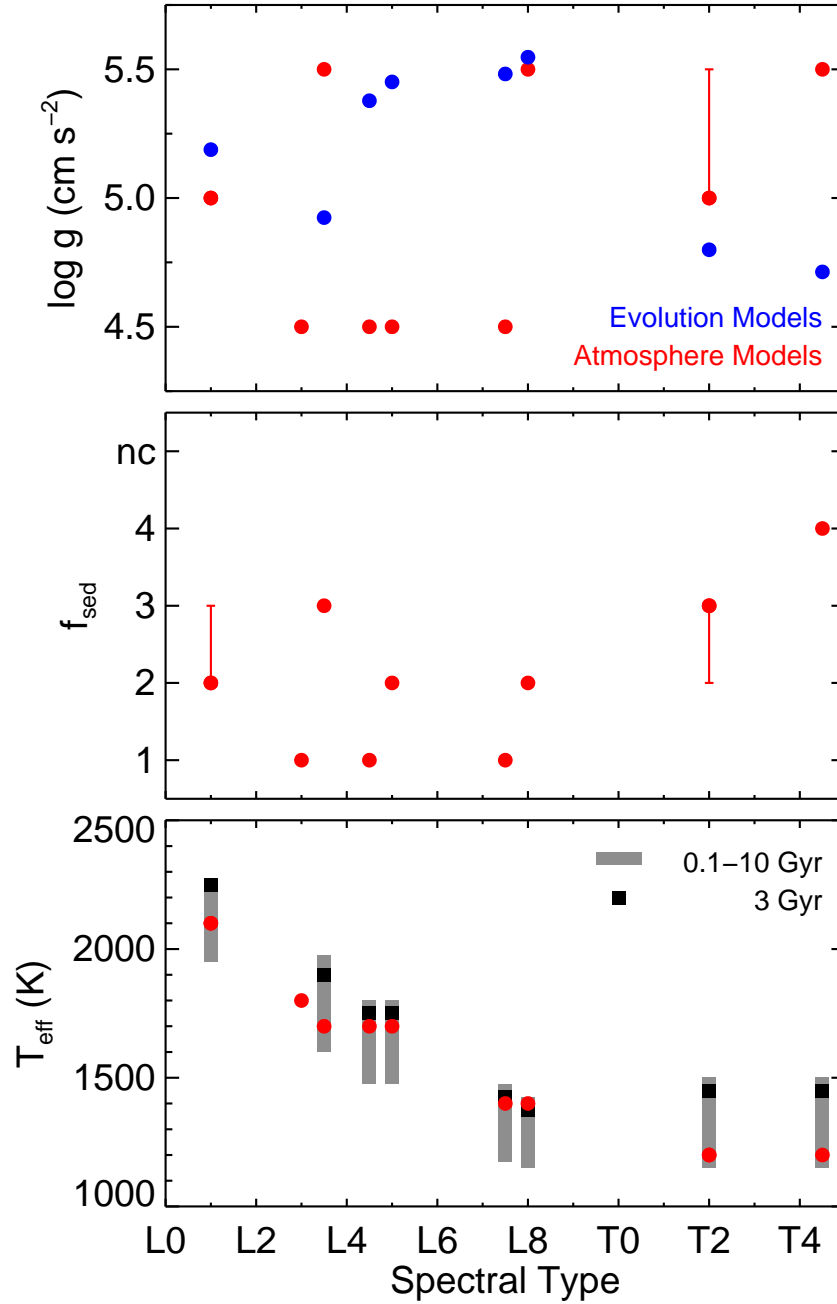


FIG. 5.— Summary of the best fitting model triplet ($T_{\text{eff}}/\log g/f_{\text{sed}}$) values over the $0.95\text{--}14.5\ \mu\text{m}$ wavelength range for each dwarf in our sample (*red circles*). Errors bars denote the range of parameters for the models with $f_{\text{MC}} > 0.1$. In the upper panel, the blue circles are the $\log g$ values derived using evolutionary models. In the lower panel, the grey regions denote the T_{eff} range corresponding to an age range of $0.1\text{--}10\ \text{Gyr}$ and the black squares denote the T_{eff} corresponding to $3\ \text{Gyr}$ (Golimowski et al. 2004). All of the T_{eff} determinations fall within the $0.1\text{--}10\ \text{Gyr}$ T_{eff} range. 2MASS 1506+1321 (L3) lacks a parallax and therefore does not have a T_{eff} range plotted.

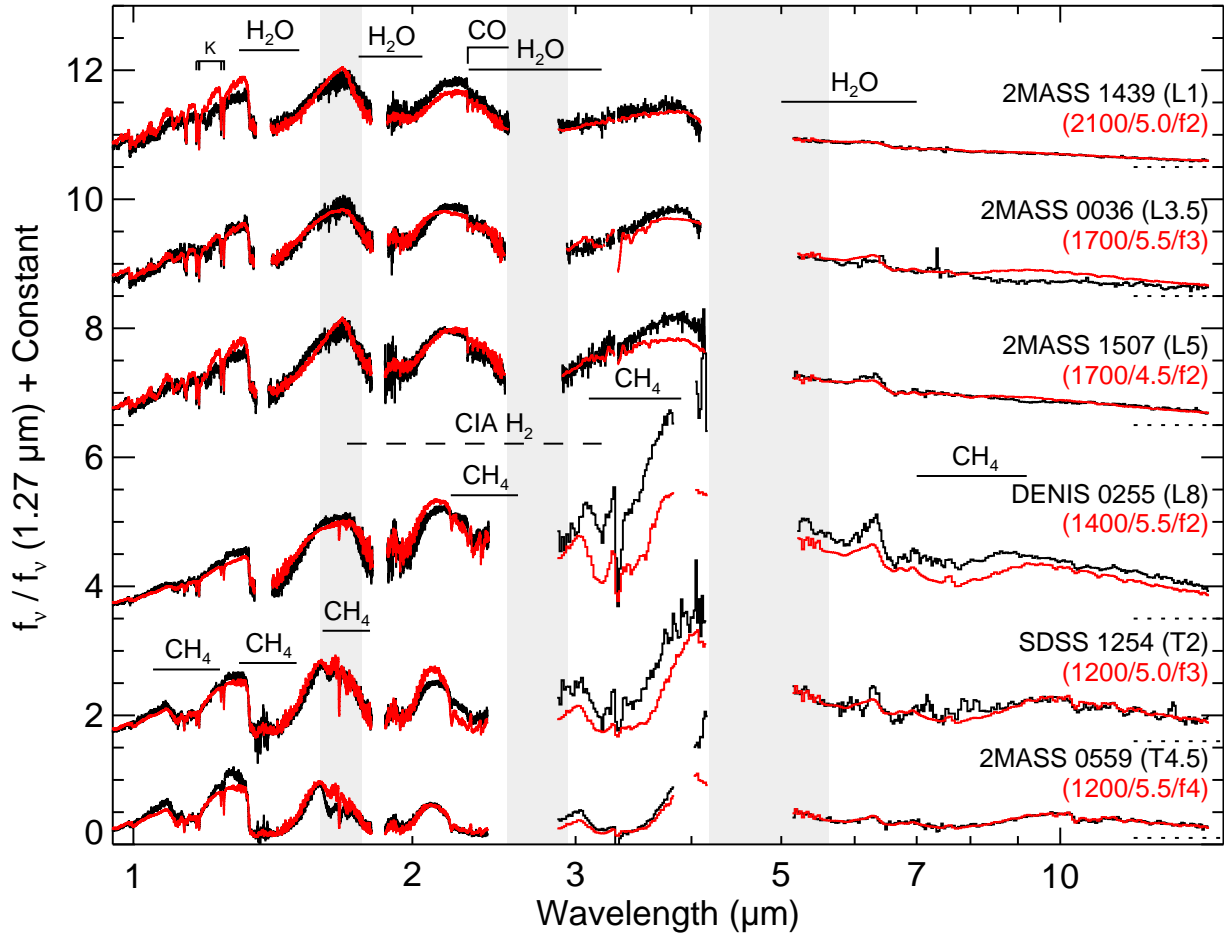


FIG. 6.— The $0.95\text{--}14.5\ \mu\text{m}$ spectra of 2MASS 1439+1929 (L1), 2MASS 0036+1821 (L3.5), 2MASS 1507–1627 (L5), DENIS 0255–4700 (L8), SDSS 1254–0122 (T2), and 2MASS 0559–1404 (T4.5) are shown in black. The data have been normalized to unity at $1.27\ \mu\text{m}$ and offset (*dotted lines*) for clarity. The best fitting models ($T_{\text{eff}}/\log g/f_{\text{sed}}$) are shown in red and have been normalized and offset with the same constants as the data. The models were multiplied by the constant C (see §4.1) before normalization to preserve the relative flux levels between the data and models. Regions not included in the fits are shown in light grey.

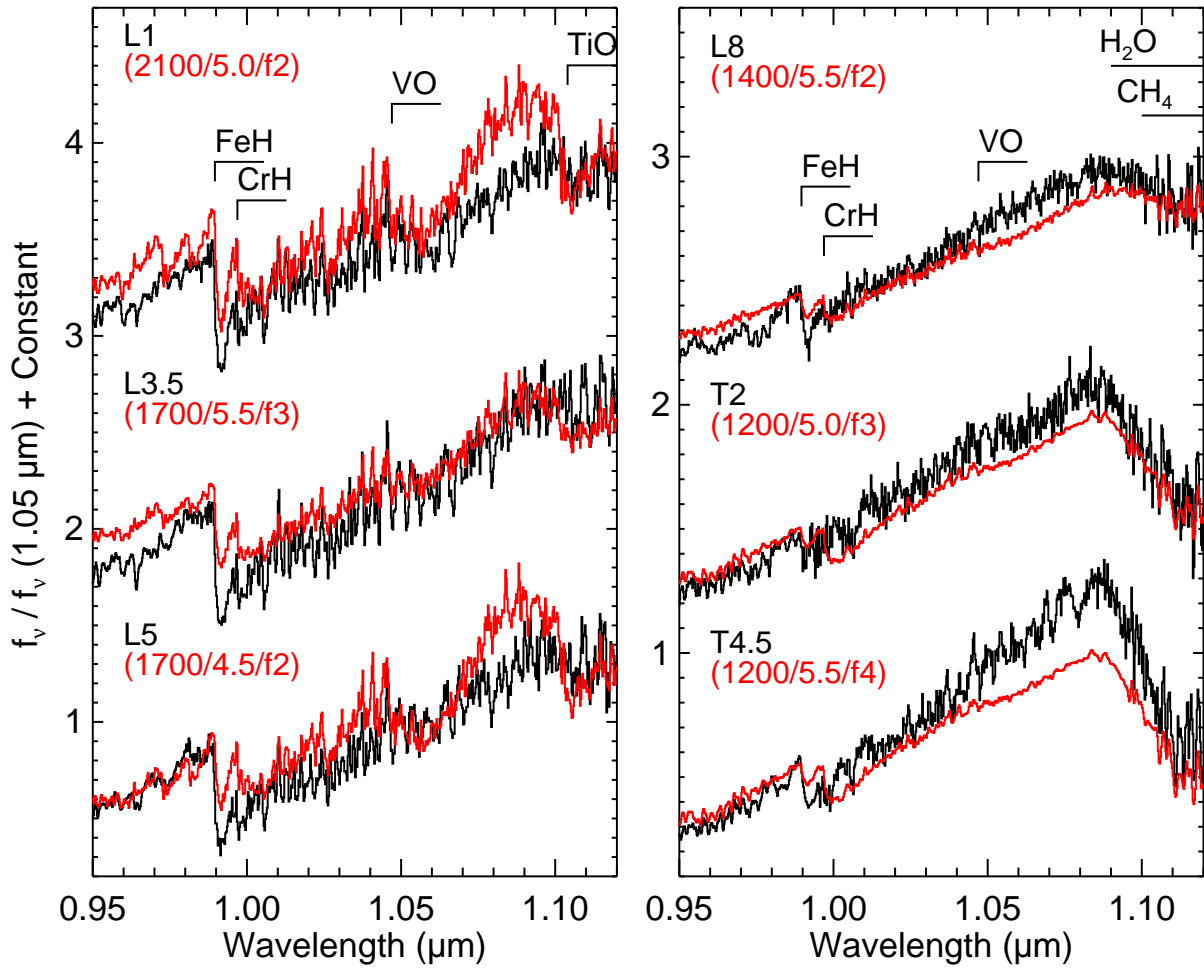


FIG. 7.— Same as Figure 6 except the data cover the Y band and were normalized at $1.05 \mu\text{m}$.

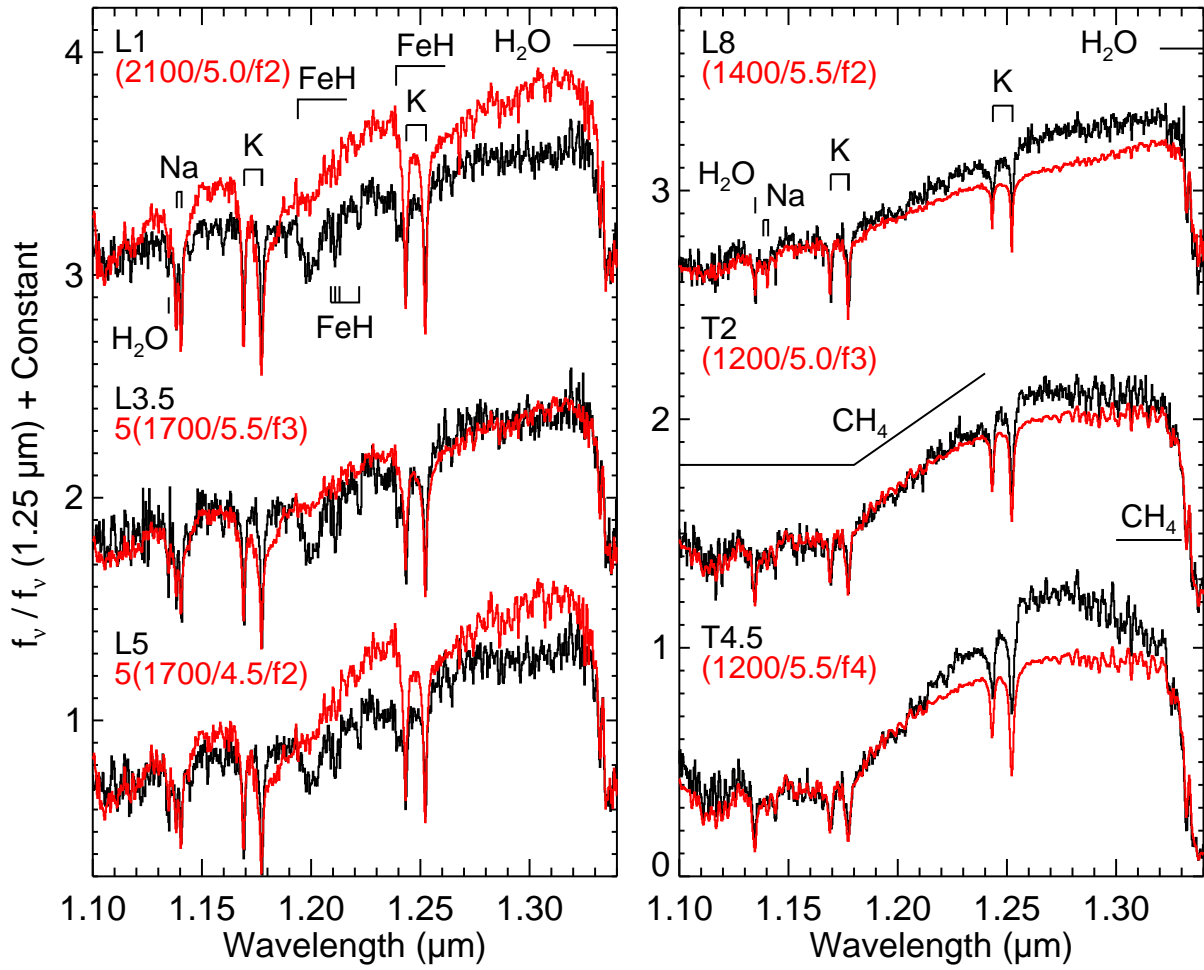


FIG. 8.— Same as Figure 6 except the data cover the *J* band and were normalized at 1.25 μm .

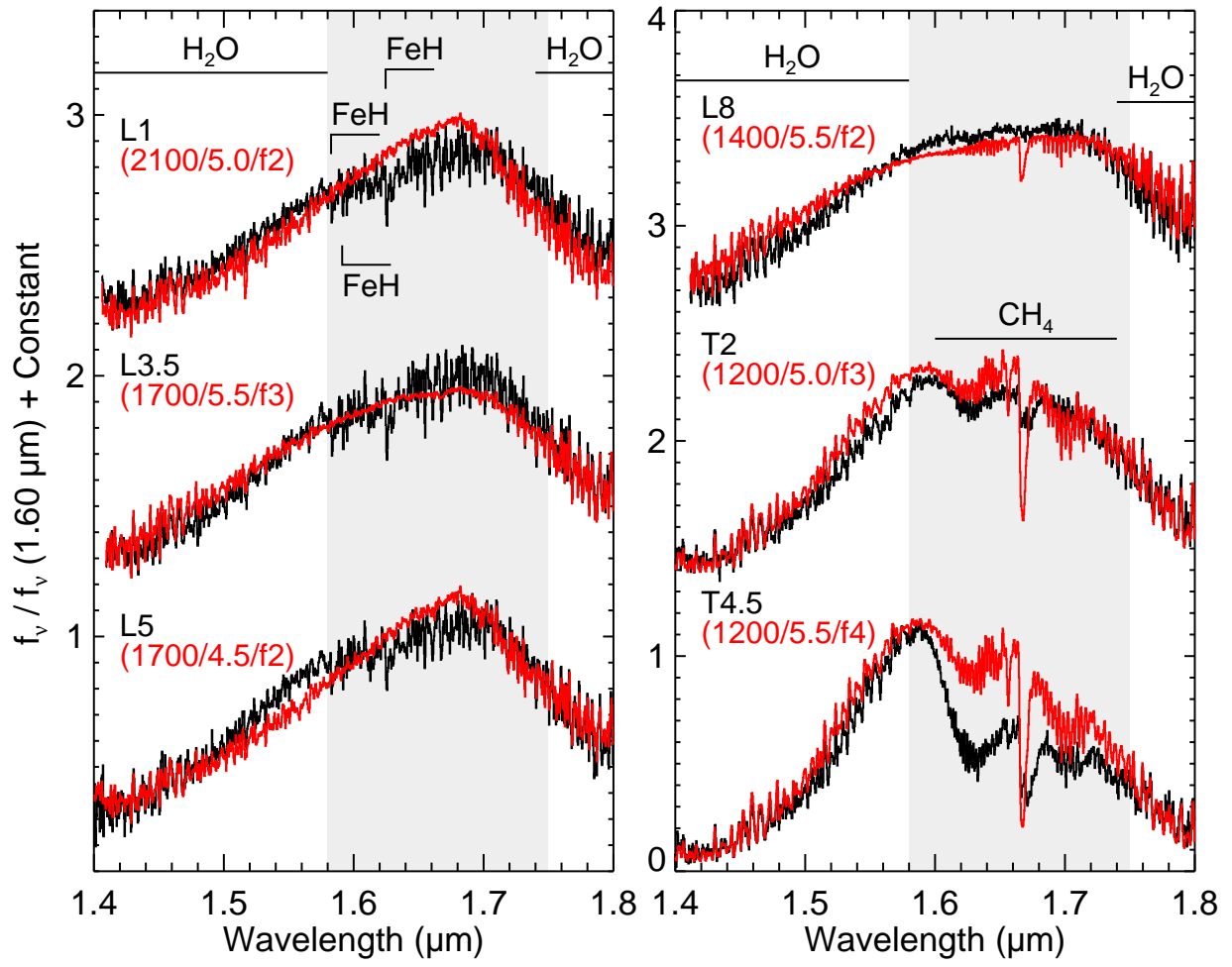


FIG. 9.— Same as Figure 6 except the data cover the H band and were normalized at 1.6 μm .

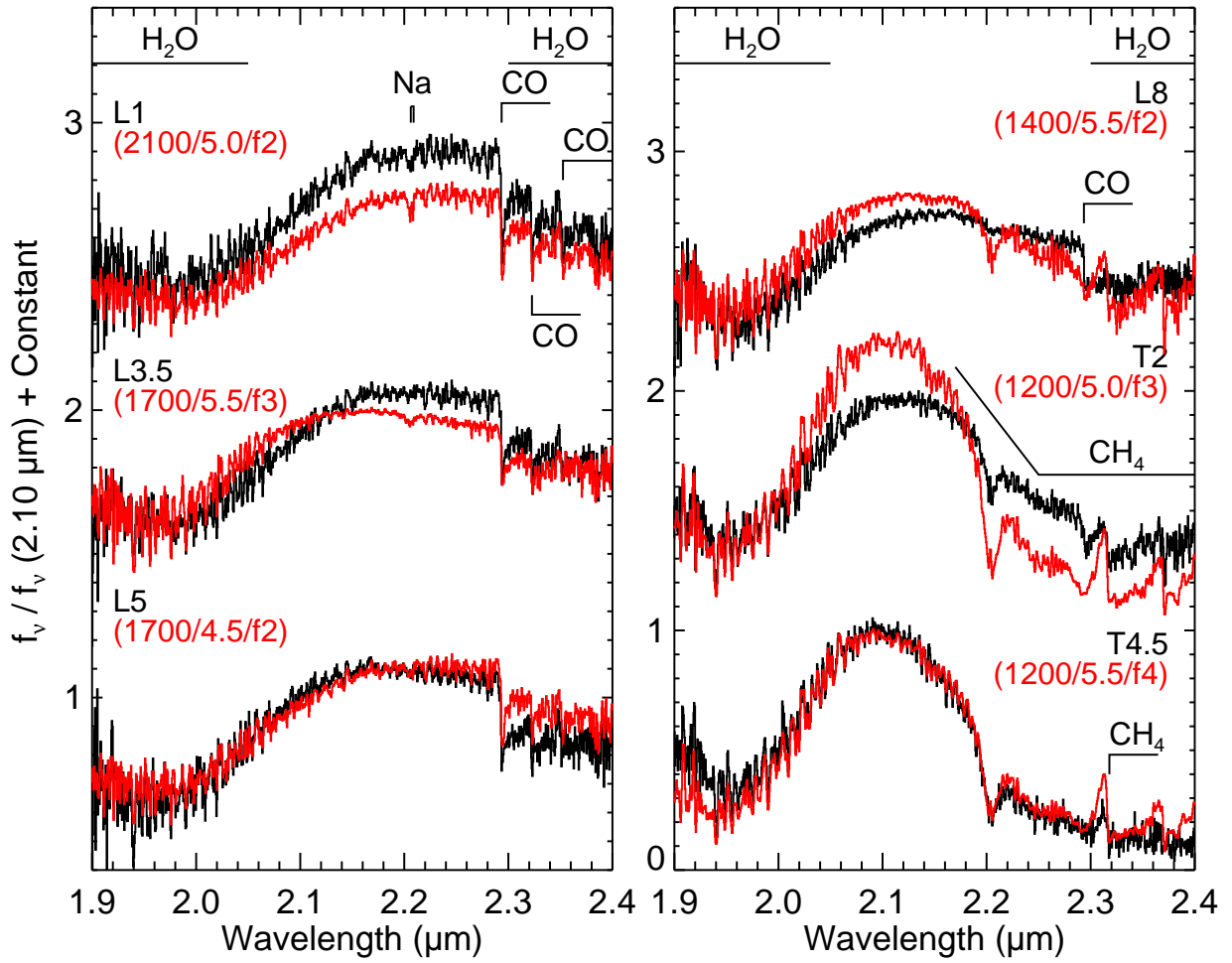


FIG. 10.— Same as Figure 6 except the data cover the *K* band and were normalized at 2.1 μm .

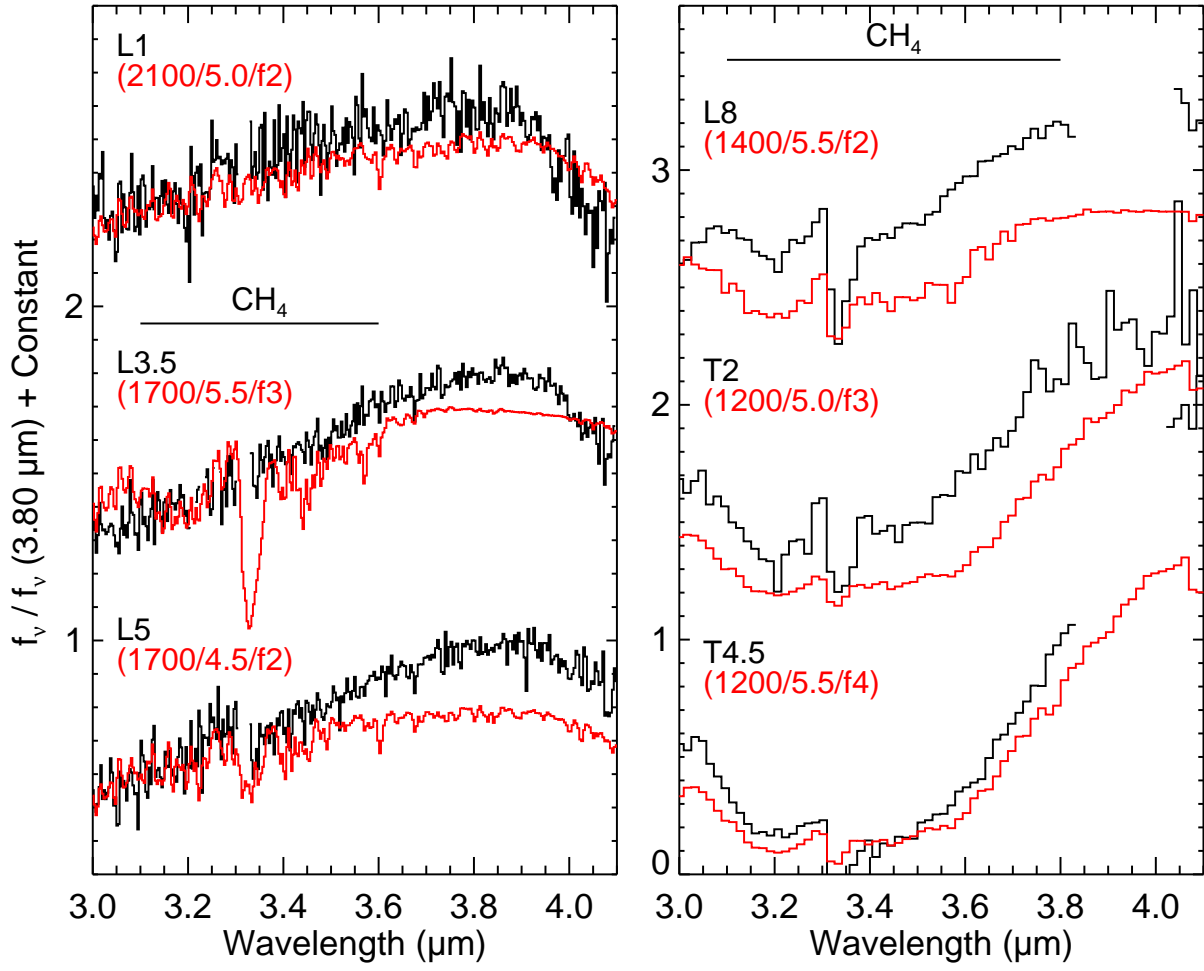


FIG. 11.— Same as Figure 6 except the data cover the L band and were normalized at $3.8 \mu\text{m}$.

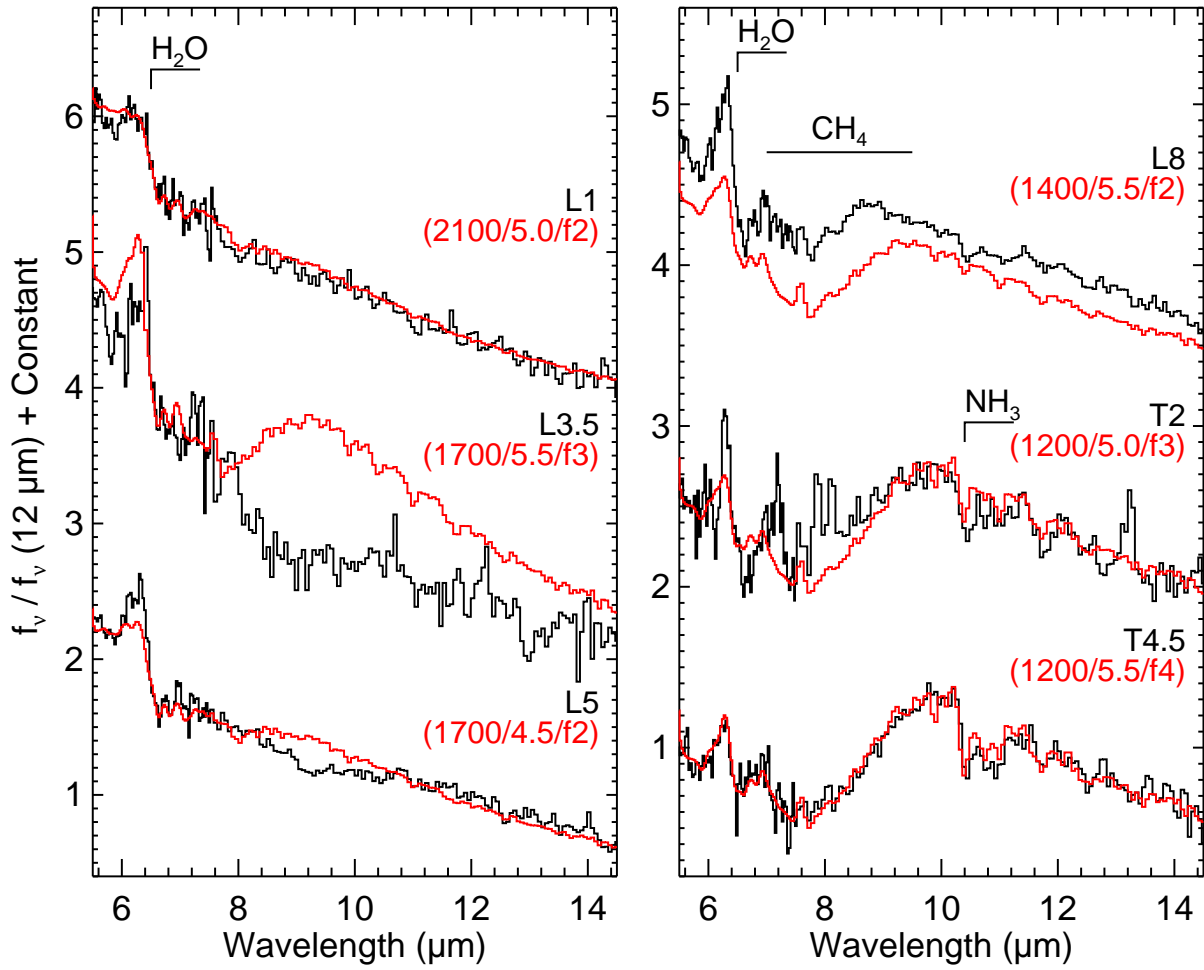


FIG. 12.— Same as Figure 6 except the data cover the IRS/SL wavelength range and were normalized at $12 \mu\text{m}$.

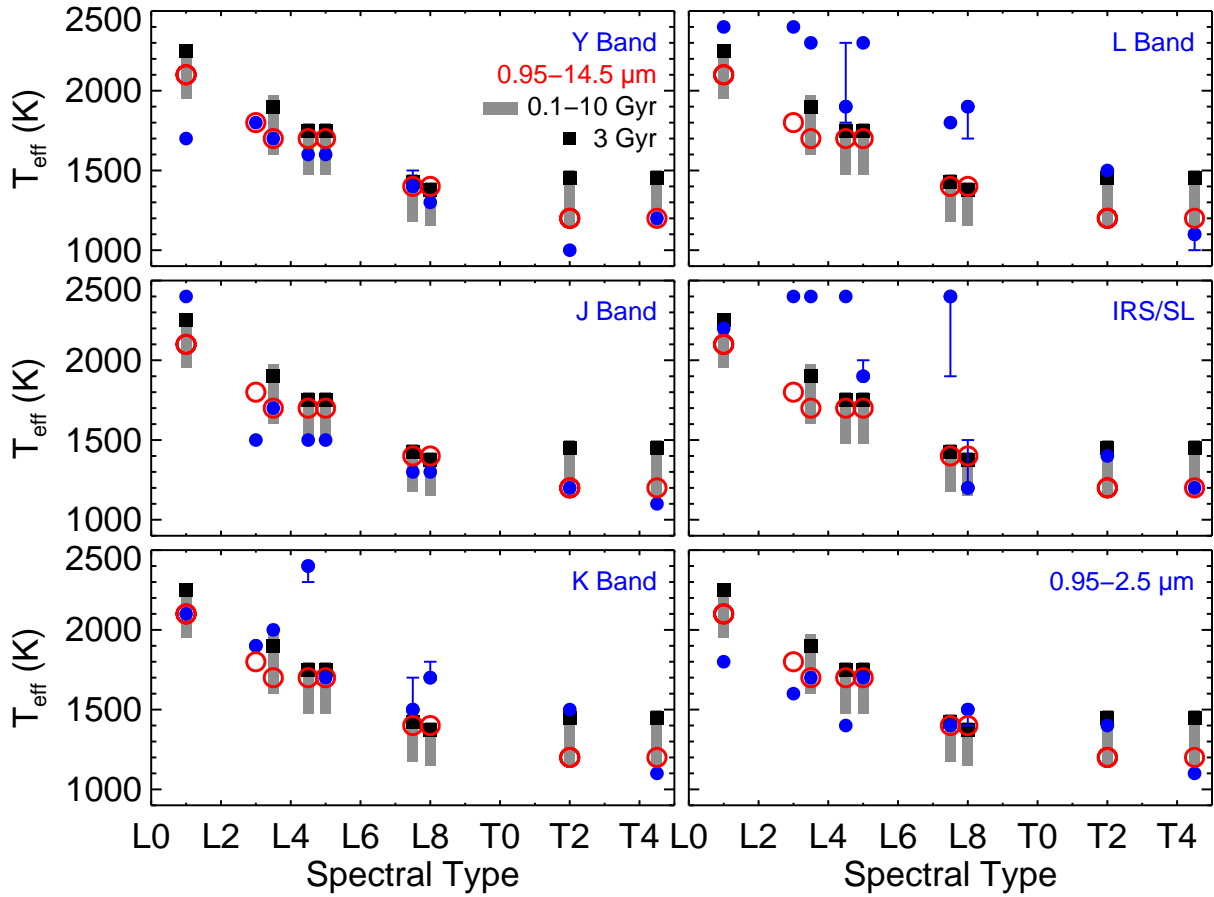


FIG. 13.— Summary of the best fitting T_{eff} values (blue circles) over the Y, J, K, and L bands as well as the IRS/SL and the 0.95–2.5 μm wavelength ranges. Shown as open red circles are the best fitting T_{eff} values derived by fitting the 0.95–14.5 μm spectra. Errors bars denote the range of T_{eff} values for the models with $f_{\text{MC}} > 0.1$. The grey regions denote the T_{eff} range corresponding to an age range of 0.1–10 Gyr and the black squares denote the T_{eff} corresponding to 3 Gyr (Golimowski et al. 2004).

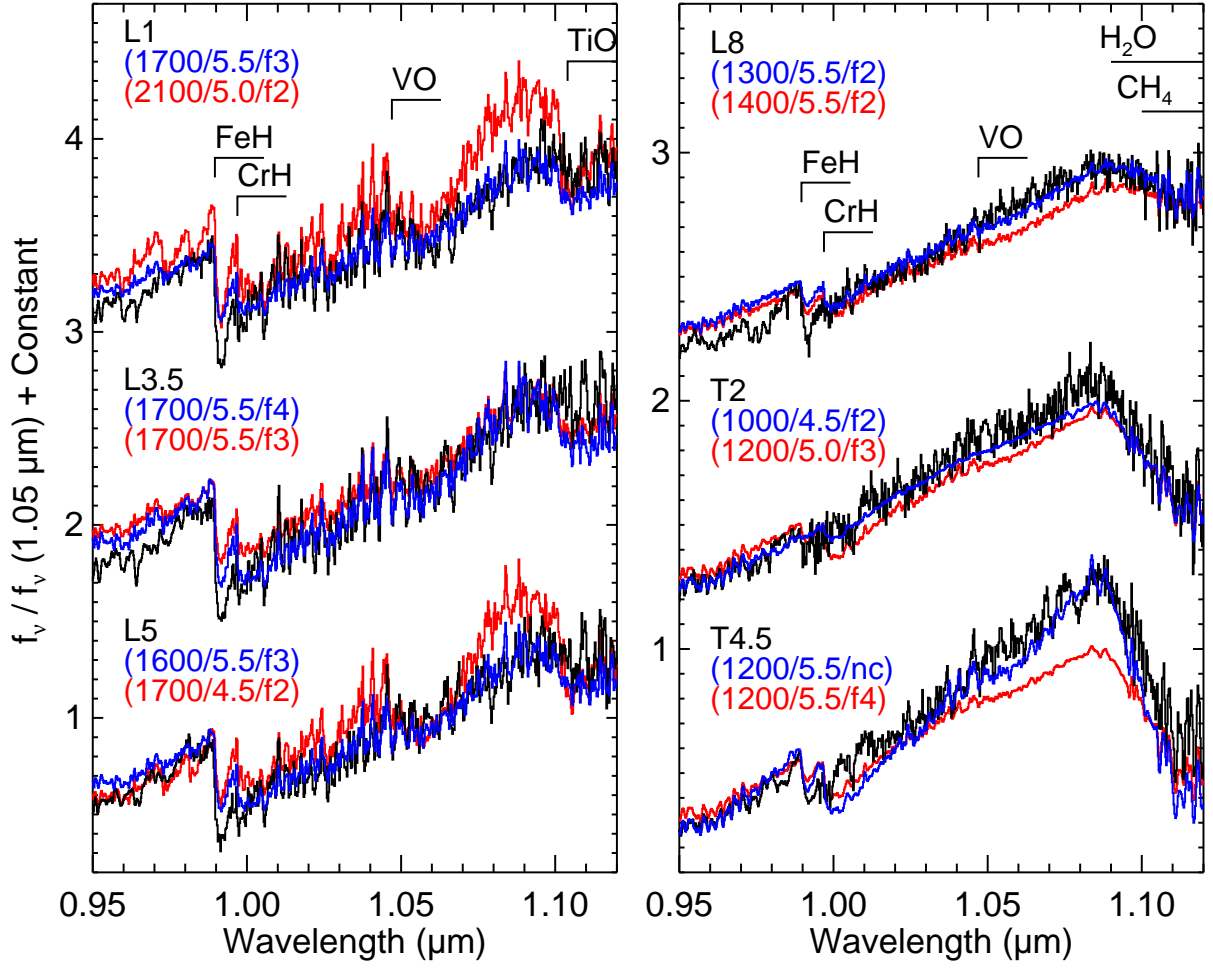


FIG. 14.— The Y-band spectra of 2MASS 1439+1929 (L1), 2MASS 0036+1821 (L3.5), 2MASS 1507–1627 (L5), DENIS 0255–4700 (L8), SDSS 1254–0122 (T2), and 2MASS 0559–1404 (T4.5) are shown in black. The data have been normalized to unity at $1.05 \mu\text{m}$ and offset for clarity. The best fitting models ($T_{\text{eff}}/\log g/f_{\text{sed}}$) are shown in blue as well as the best fitting models (*red*) obtained from fitting the entire $0.95\text{--}14.5 \mu\text{m}$ spectrum. The models have been normalized and offset with the same constants as the data and were multiplied by the constant C (see §4.1) before normalization to preserve the relative flux levels between the data and models.

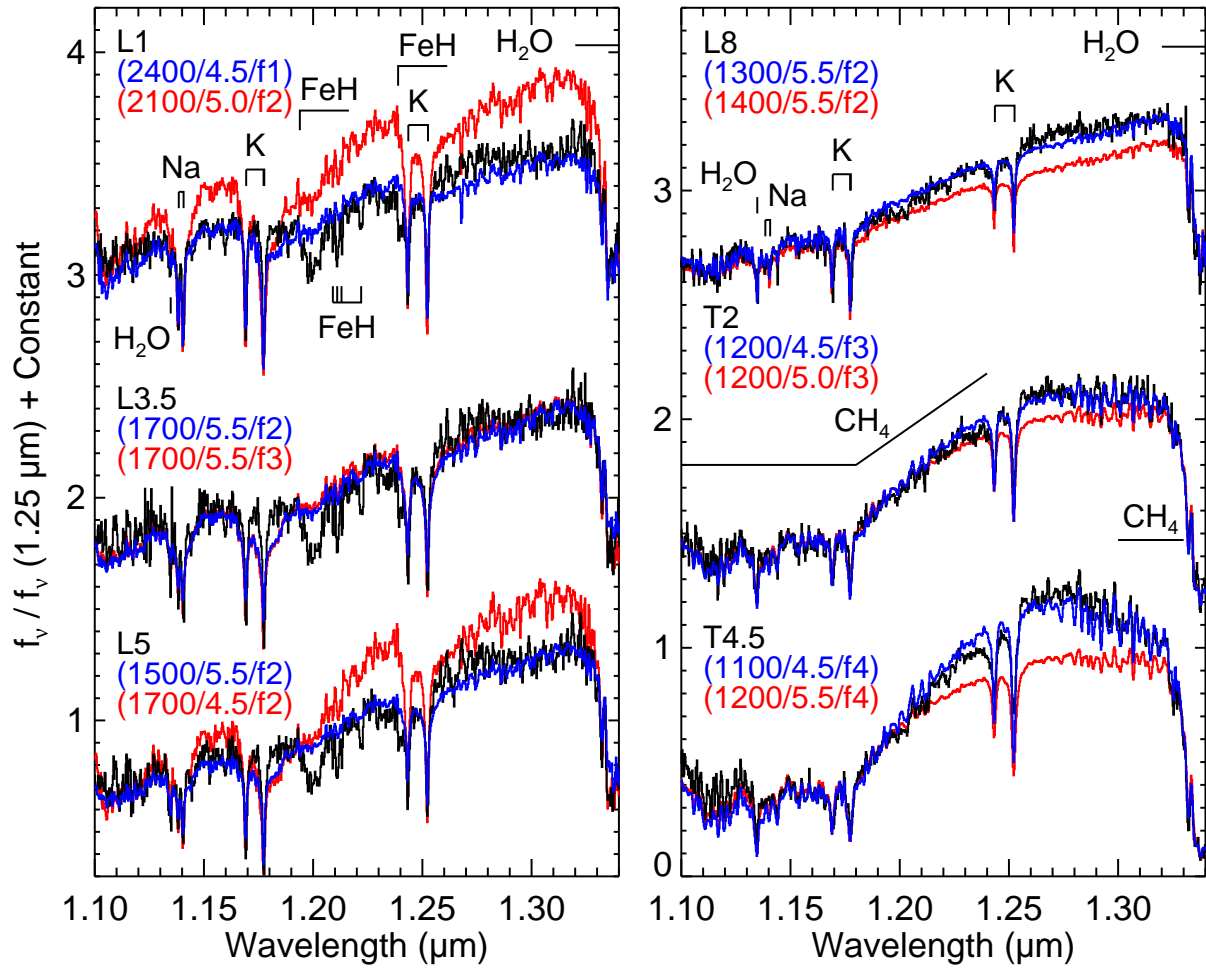


FIG. 15.— Same as Figure 14 except the data cover the J band and were normalized at 1.25 μm .

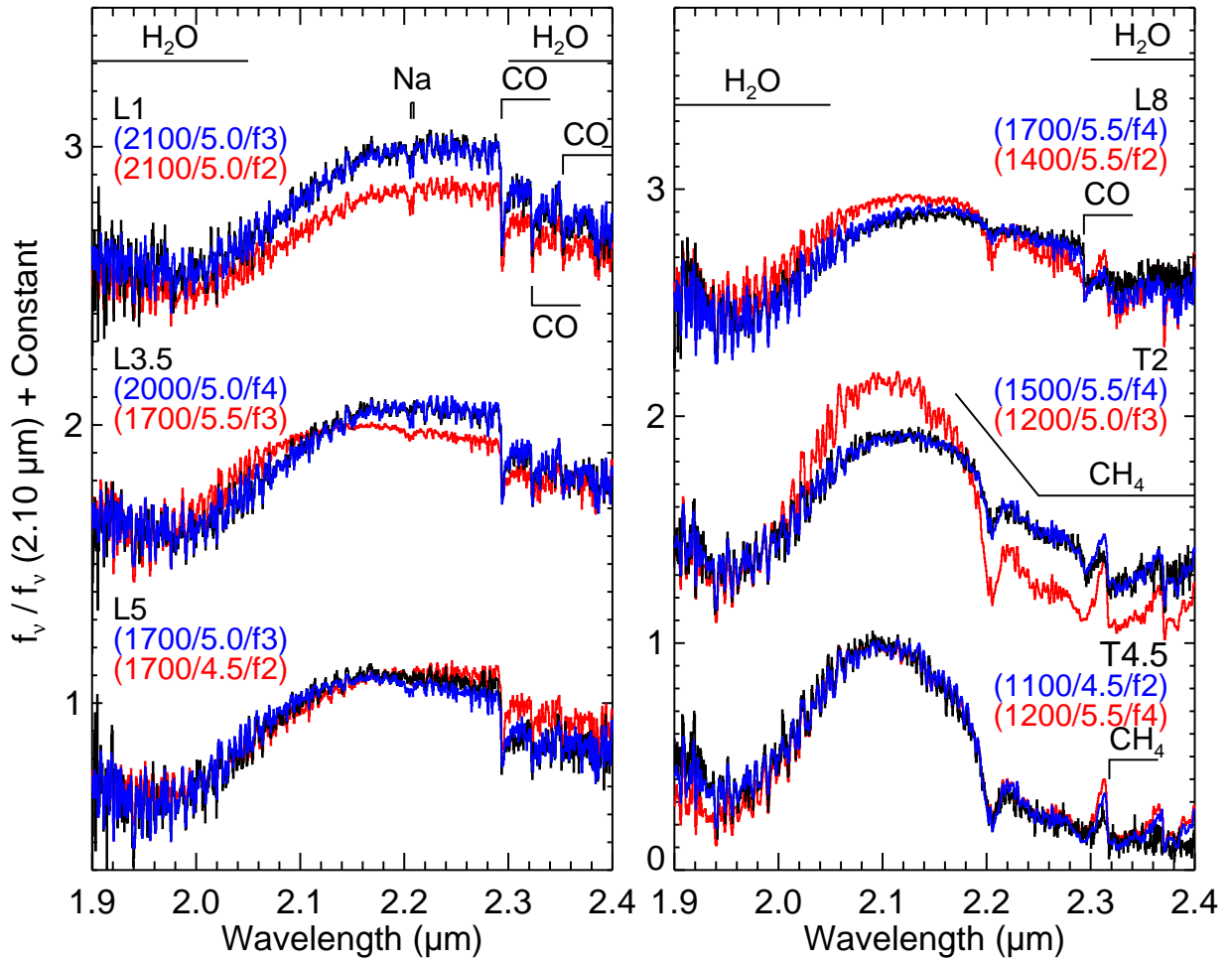


FIG. 16.— Same as Figure 14 except the data cover the *K* band and were normalized at 2.1 μm .

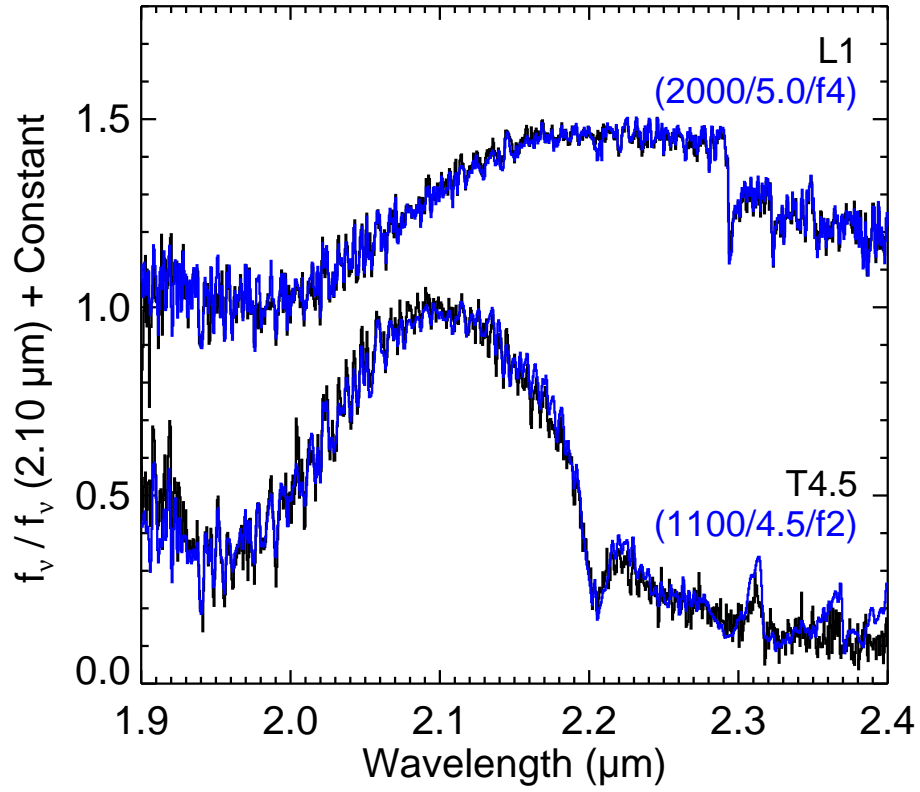


FIG. 17.— The K -band spectra of 2MASS 1439+1929 (L1) and 2MASS 0559–1404 (T4.5) are shown in black. The data have been normalized to unity at $2.1 \mu\text{m}$ and offset for clarity. The best fitting models ($T_{\text{eff}}/\log g/f_{\text{sed}}$) are shown in blue. The models have been normalized and offset with the same constants as the data and were multiplied by the constant C (see §4.1) before normalization to preserve the relative flux levels between the data and models.

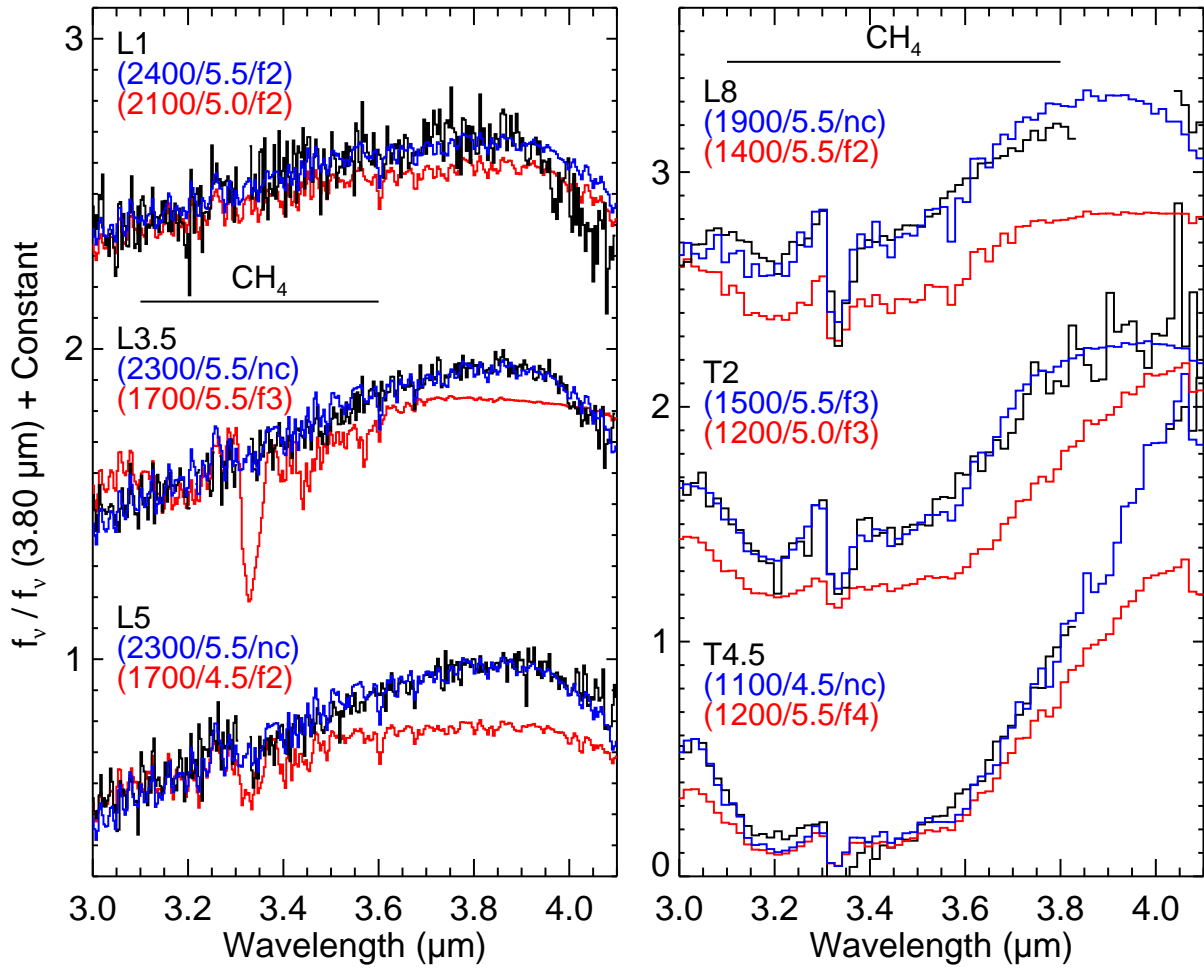


FIG. 18.— Same as Figure 14 except the data cover the L band and were normalized at 3.8 μm .

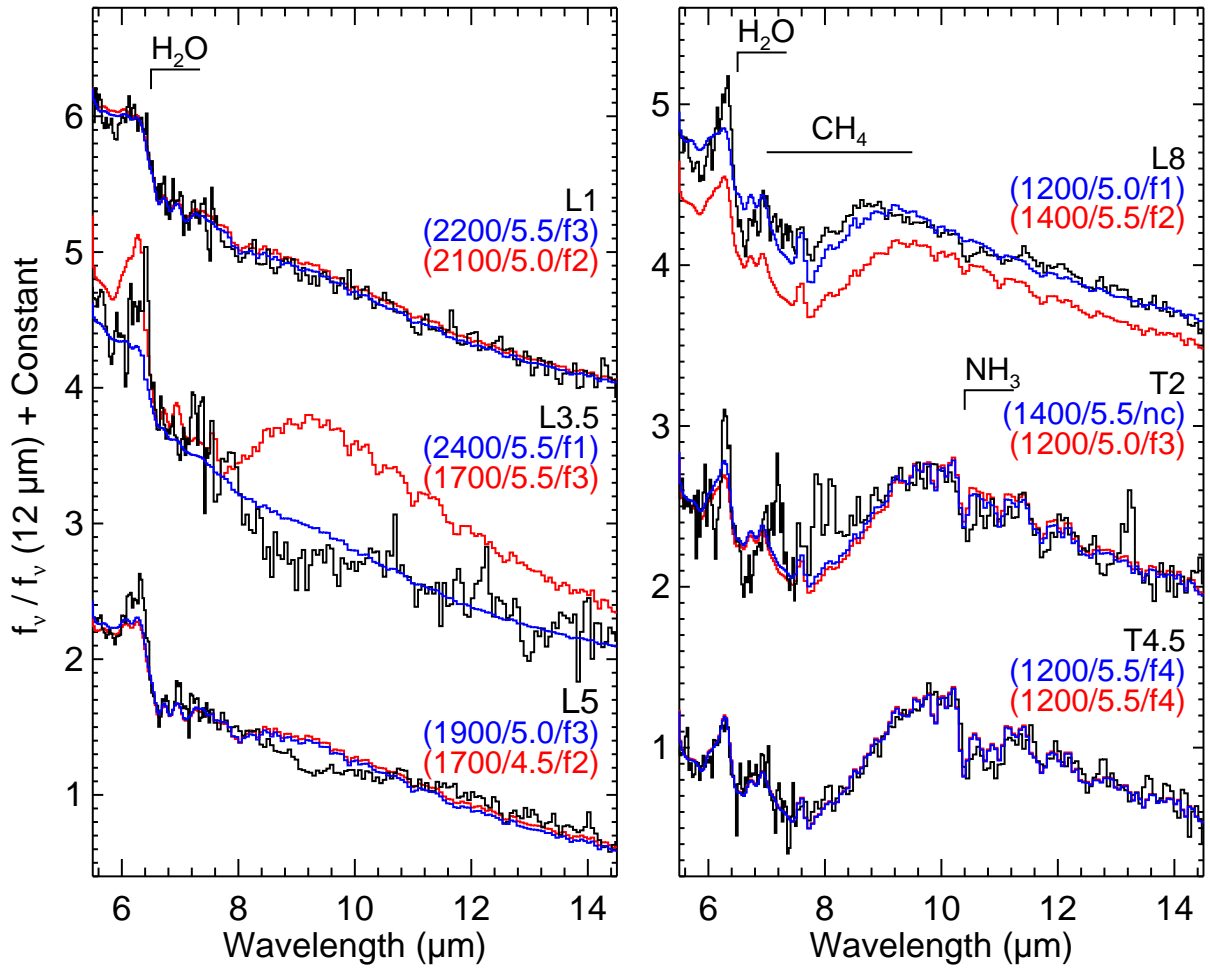


FIG. 19.— Same as Figure 14 except the data cover the IRS/SL wavelength range and were normalized at $12 \mu\text{m}$.

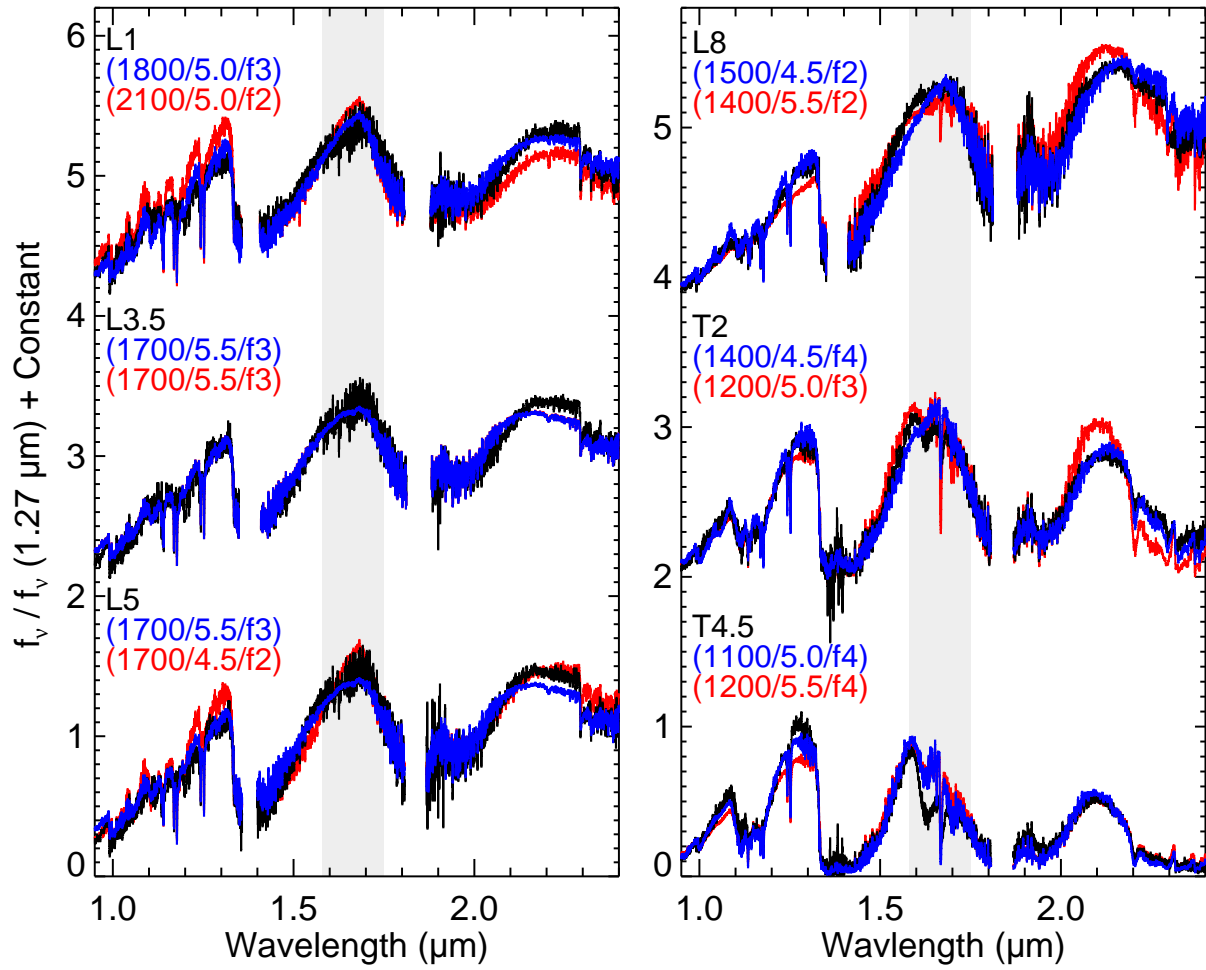


FIG. 20.— Same as Figure 14 except the data cover the 0.95–2.5 μm wavelength range and were normalized at 1.27 μm .

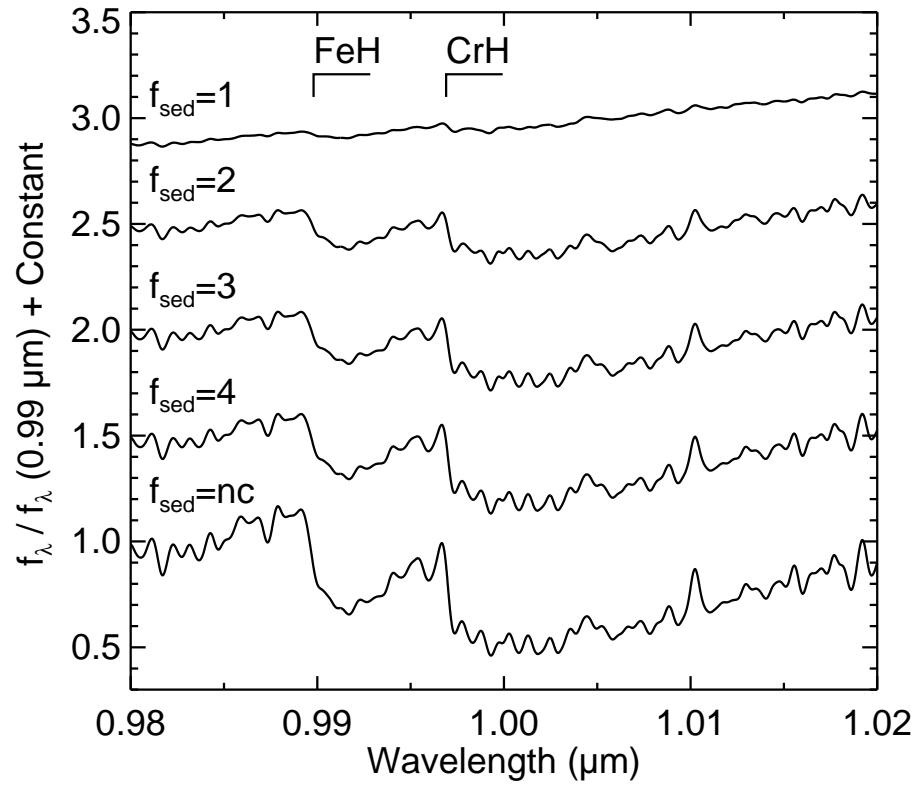


FIG. 21.— Synthetic spectra smoothed to $R=2000$ with $T_{\text{eff}}=1400$ K, $\log g=5.0$, and $f_{\text{sed}}=1, 2, 3, 4$, and the nc model. The depth of the FeH bandhead at $0.9896 \mu\text{m}$ increases as f_{sed} increases in value.

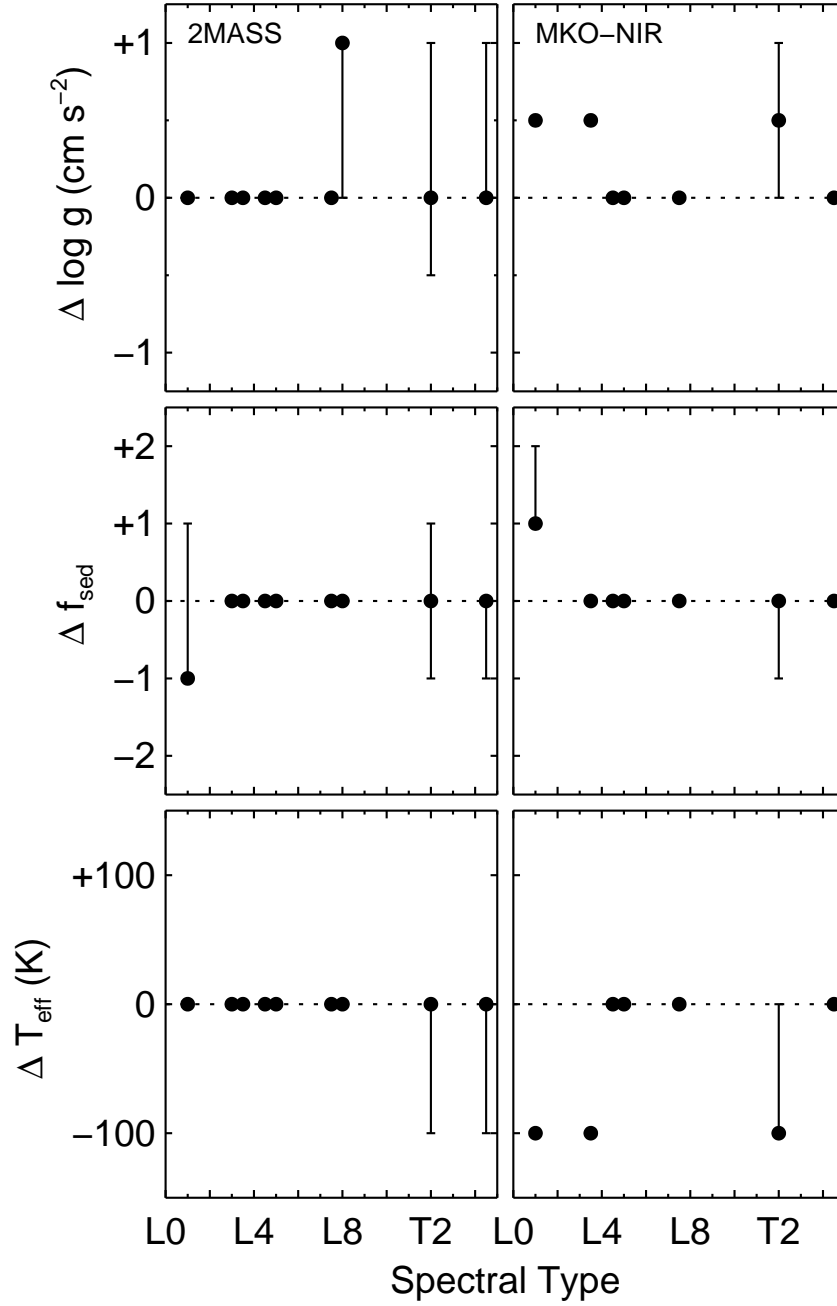


FIG. 22.— Effects of different absolute flux calibrations on the derived atmospheric parameters over the $0.95\text{--}14.5\ \mu\text{m}$ wavelength range. The panels show the difference between the values derived after scaling the near-infrared spectra by a single scale factor and the values derived after scaling the J , H , and K band spectra separately using 2MASS (*left*) and MKO-NIR (*right*) photometry.

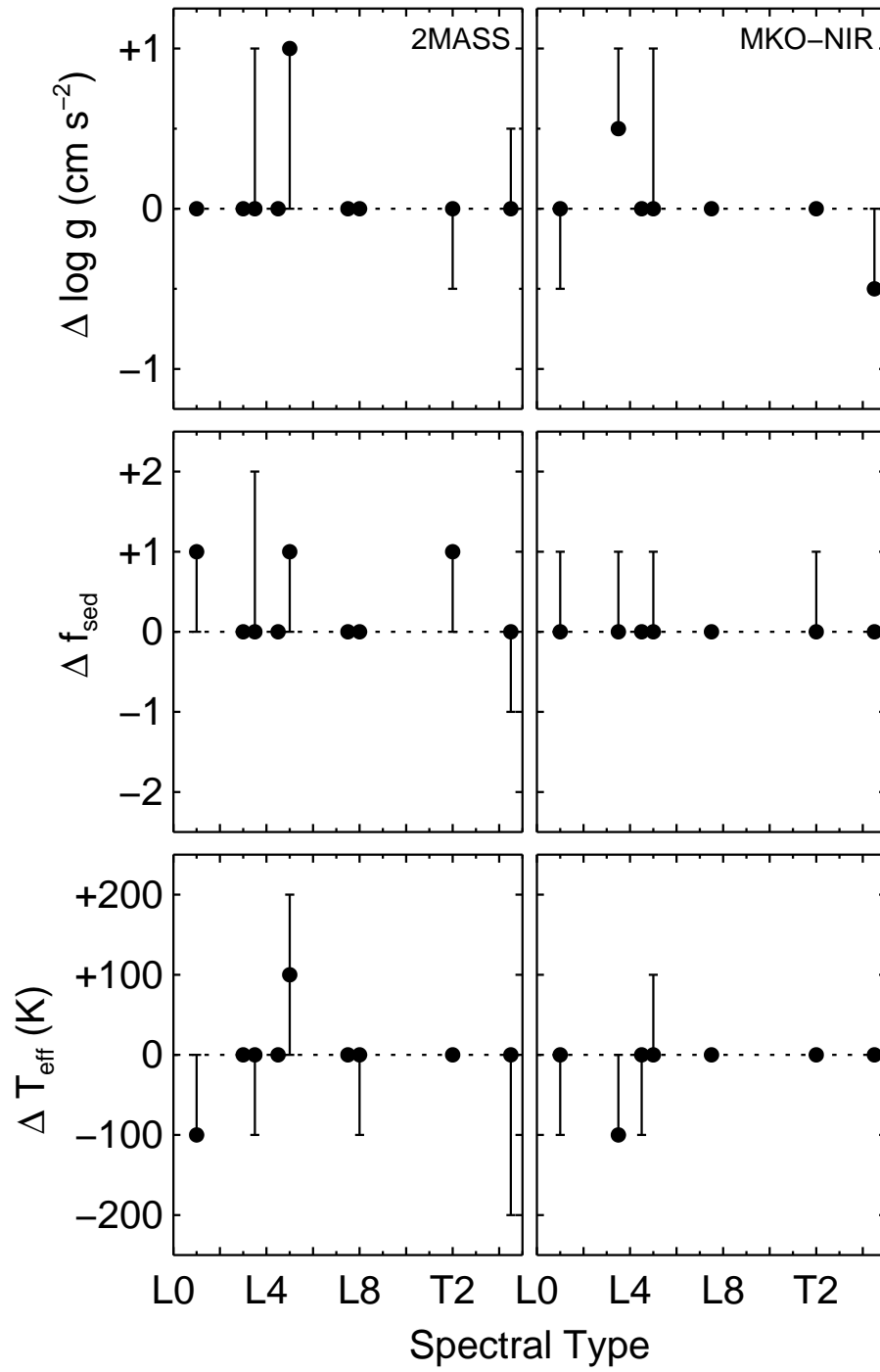


FIG. 23.— Same as Figure 22 except the data were only fit from 0.95 to 2.5 μm .

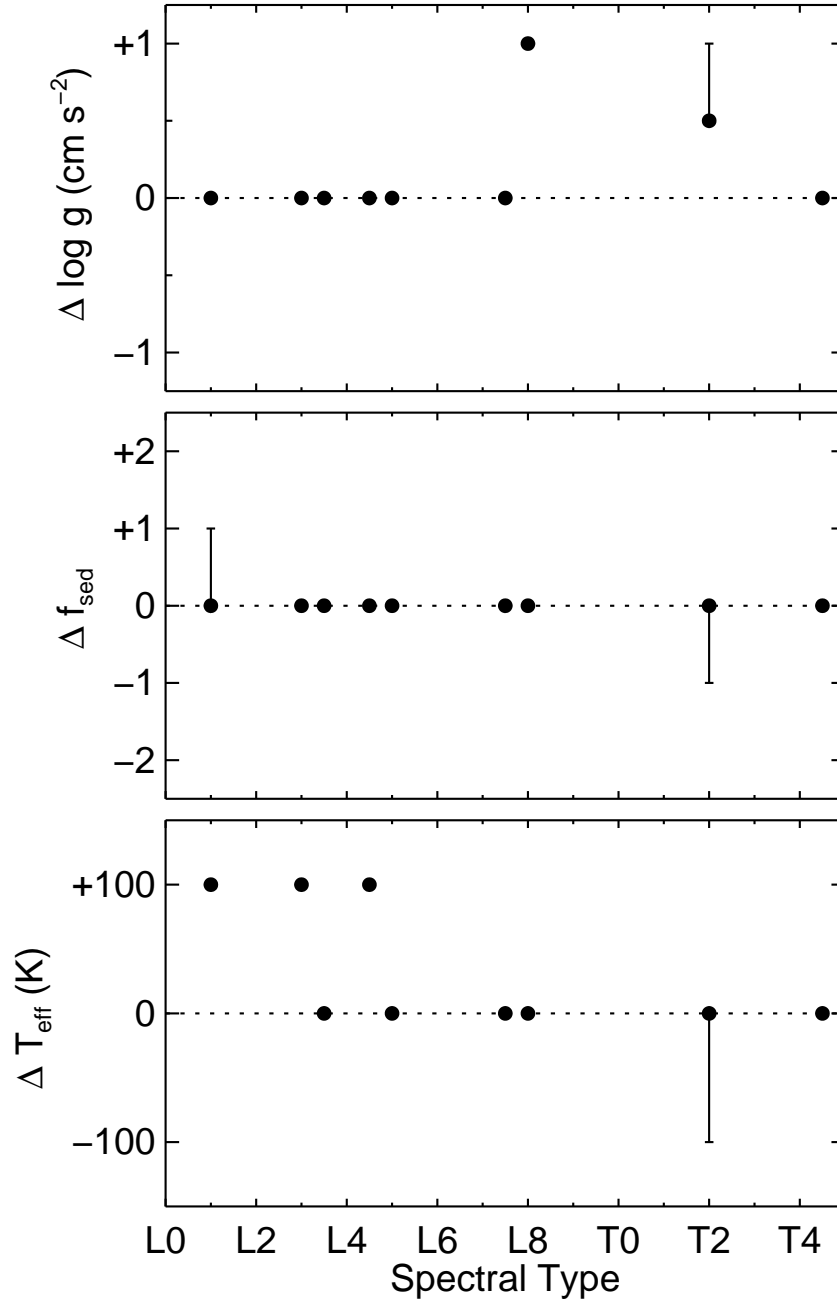


FIG. 24.— Effects of different weighting schemes on the derived atmospheric parameters over the 0.95–14.5 μm wavelength range. The panels show the difference between the values derived by setting the weights to $w_i = \Delta\lambda_i$ and the values derived by setting the weights to $w_i = 1/n$ where n is the number of pixels in bins of width $\delta \ln \lambda = 0.01$.

TABLE 1
THE PROPERTIES OF THE L AND T DWARFS IN OUR SAMPLE

Object	Spectral Type ^a		J^b (mag)	$J - H$ (mag)	$H - K_s$ (mag)	$J - K_s$ (mag)	π^c (mas)	Ref.
	Optical	Infrared						
2MASS J14392836+1929149	L1	L1	12.759±0.019	0.718±0.027	0.495±0.029	1.213±0.029	69.6±0.5	1
2MASS J15065441+1321060	L3	...	13.365±0.023	0.985±0.031	0.639±0.028	1.624±0.030
2MASS J00361617+1821104	L3.5	L4±1	12.466±0.027	0.878±0.040	0.530±0.036	1.408±0.034	114.2±0.8	1
2MASS J22244381-0158521	L4.5	L3.5	14.073±0.027	1.255±0.037	0.796±0.035	2.051±0.035	87.02±0.89	1,2
2MASS J15074769-1627386	L5	L5.5	12.830±0.027	0.935±0.036	0.583±0.035	1.518±0.037	136.4±0.6	1
2MASS J08251968+2115521	L7.5	L6	15.100±0.034	1.308±0.047	0.764±0.041	2.072±0.043	94.22±0.99	1,2
DENIS 025503.3-470049.0	L8	L9	13.246±0.027	1.042±0.036	0.646±0.034	1.688±0.036	201.37±3.89	3
SDSS J125453.90-012247.4	T2	T2	14.891±0.035	0.801±0.043	0.253±0.060	1.054±0.064	73.96±1.59	2,4
2MASS J05591914-1404488	T5	T4.5	13.802±0.024	0.123±0.050	0.102±0.068	0.225±0.057	96.73±0.96	1,2

REFERENCES. — (1) Dahn et al. (2002), (2) Vrba et al. (2004), (3) Costa et al. (2006), and (4) Tinney et al. (2003)

^a Spectral types of the L dwarfs are from Kirkpatrick et al. (1999, 2000), Reid et al. (2000), Gizis et al. (2000), Geballe et al. (2002), Knapp et al. (2004), Burgasser et al. (2006a), and J.D. Kirkpatrick (in preparation). Spectral types of the T dwarfs are from Burgasser et al. (2006a). Errors on spectral types are ±0.5 subclass unless otherwise noted.

^b J -, H -, and K_s -band photometry is from the 2MASS Point Source Catalog.

^c Based on the weighted mean of the referenced parallaxes (Golimowski et al. 2004)

TABLE 2
SPECTRAL CHARACTERISTICS OF ULTRACOOL DWARFS IN OUR SAMPLE

Object	$R=\lambda/\Delta\lambda$				Ref.
	(0.6–0.9 μm)	(0.9–2.5 μm)	(3.0–4.1 μm)	(5.5–14.5 μm)	
2MASS J1439+1929	890	2000	940	90	1,2,2,3
2MASS J1506+1321	890	2000	940	90	4,2,2,3
2MASS J0036+1821	890	2000	940	90	5,2,2,3
2MASS J2224–0158	890	2000	425	90	6,2,2,3
2MASS J1507–1627	890	2000	940	90	5,2,2,3
2MASS J0825+2115	890	1200	210	90	6,2,2,3
DENIS 0255–4700	890	2000	210	90	7,2,2,3
SDSS J1254–0122	1200	1200	210	90	8,2,2,3
2MASS J0559–1404	1200	1200	210	90	8,2,2,3

REFERENCES. — (1) Kirkpatrick et al. (1999); (2) Cushing et al. (2005); (3) Cushing et al. (2006); (4) Gizis et al. (2000); (5) Reid et al. (2000); (6) Kirkpatrick et al. (2000); (7) Kirkpatrick (2007, private communication); (8) Burgasser et al. (2003a)

TABLE 3
DERIVED PARAMETERS FOR L AND T DWARFS (0.9–14.5 μM)

Object	Spectral Type ^a		Atmospheric Parameters								
			By Spectral Fitting				By Evolutionary Sequences			Golimowski et al. T_{eff} (K)	
	Optical	Infrared	T_{eff} (K)	$\log g$ (cm s ⁻²)	f_{sed}	f_{MC}	$\log g$ (cm s ⁻²)	0.1 Gyr	3 Gyr	10 Gyr	
2MASS J1439+1929	L1	L1	2100	5.0	2	0.582	5.188	1950	2250	2275	
			2100	5.0	3	0.418	5.188	1950	2250	2275	
2MASS J1506+1321	L3	...	1800	4.5	1	1.000	
2MASS J0036+1821	L3.5	L4±1	1700	5.5	3	1.000	4.924	1650	1900	1975	
2MASS J2224-0158	L4.5	L3.5	1700	4.5	1	0.999	5.378	1475	1750	1800	
2MASS J1507-1627	L5	L5.5	1700	4.5	2	1.000	5.451	1475	1750	1800	
2MASS J0825+2115	L7.5	L6	1400	4.5	1	1.000	5.482	1175	1425	1475	
DENIS 0255-4700	L8	L9	1400	5.5	2	0.988	5.547	1150 ^b	1375	1425	
SDSS J1254-0122	T2	T2	1200	5.0	3	0.831	4.799	1150	1425	1500	
			1200	5.5	2	0.105	4.908	1150	1425	1500	
2MASS J0559-1404	T5	T4.5	1200	5.5	4	0.999	4.713	1150	1425	1500	

NOTE. — Only models with $f_{\text{MC}} > 0.1$ are listed.

^a Spectral types of the L dwarfs are from Kirkpatrick et al. (1999), Reid et al. (2000), Gizis et al. (2000), Kirkpatrick et al. (2000), Burgasser et al. (2006a), and J.D. Kirkpatrick (in preparation). Spectral types of the T dwarfs are from Burgasser et al. (2003a, 2006a). Errors on spectral types are ± 0.5 subclass unless otherwise noted.

^b DENIS 0255-4700 was not included in the Golimowski et al. (2004) sample. We have computed its L_{bol} using the new parallax measurement of Costa et al. (2006). The bolometric flux was determined by integrating over its 0.6 to 14.5 μm spectrum as described in Cushing et al. (2006).

TABLE 4
THE PROPERTIES OF SDSS 1254–0122 AND 2MASS 0559–1404

Parameter	SDSS 1254–0122		2MASS 0559–1404	
	single	equal mass binary	single	equal mass binary
$\log (L_{\text{bol}}/L_{\odot})$	–4.60	–4.90	–4.63	–4.93
T_{eff} (K)	1200	<1160	1200	<1150
$\log g$ (cm s^{-2})	4.71	<5.38	4.80	<5.38
Age (Gyr)	~ 0.3	<10	~ 0.4	< 10

TABLE 5
DERIVED PARAMETERS OF THE L AND T DWARFS FROM RESTRICTED SPECTRAL INTERVALS

Object	Spectral Type ^a		$T_{\text{eff}}(\text{K}) / \log g(\text{cm s}^{-2}) / f_{\text{sed}} / f_{\text{MC}}$					
	Optical	Infrared	<i>Y</i>	<i>J</i>	<i>K</i>	<i>L</i>	IRS/SL	Near-Infrared
2MASS 1439+1929	L1	L1	1700/5.5/3/1.000	2400/4.5/1/1.000	2100/5.0/3/1.000	2400/5.5/2/0.922	2200/5.5/3/0.922	1800/5.0/3/1.000
2MASS 1506+1321	L3	...	1800/5.5/4/1.000	1500/5.5/1/1.000	1900/4.5/3/0.761	2400/5.5/4/0.997	2400/5.5/1/1.000	1600/4.5/2/1.000
			1900/4.5/2/0.240
2MASS 0036+1821	L3.5	L4±1	1700/5.5/4/0.988	1700/5.5/2/1.000	2000/5.0/4/1.000	2300/5.5/nc/1.000	2400/5.5/1/0.863	1700/5.5/3/1.000
2MASS 2224-0158	L4.5	L3.5	1600/5.5/3/0.996	1500/5.0/1/1.000	2400/5.5/nc/0.748	1900/4.5/4/0.219	2400/5.5/1/1.000	1400/4.5/1/1.000
			2300/5.0/nc/0.133	2200/5.5/nc/0.190
			2300/5.5/nc/0.122
			1800/5.0/4/0.114
2MASS 1507-1627	L5	L5.5	1600/5.5/3/1.000	1500/5.5/2/0.999	1700/5.0/3/1.000	2300/5.5/nc/1.000	1900/5.0/3/0.627	1700/5.5/3/1.000
			2000/5.0/3/0.370	...
2MASS 0825+2115	L7.5	L6	1400/5.5/2/0.549	1300/4.5/1/0.984	1500/4.5/2/0.835	1800/5.0/4/0.998	2400/5.5/nc/0.201	1400/4.5/1/1.000
			1500/5.0/2/0.359	...	1700/5.0/3/0.166	...	2200/5.5/4/0.166	...
			2300/5.5/nc/0.157	...
			1900/5.5/4/0.142	...
DENIS 0255-4700	L8	L9	1300/5.5/2/0.992	1300/5.5/2/0.999	1700/5.5/4/0.820	1900/5.5/nc/0.447	1200/5.5/1/0.465	1500/4.5/2/0.572
			1800/5.5/4/0.177	1700/5.5/4/0.241	1500/4.5/2/0.218	1400/4.5/2/0.428
			1700/5.0/4/0.186	1200/5.0/1/0.167	...
SDSS 1254-0122	T2	T2	1000/4.5/2/1.000	1200/4.5/3/1.000	1500/5.5/4/1.000	1500/5.5/3/0.918	1400/5.5/nc/0.910	1400/4.5/4/1.000
2MASS 0559-1404	T4.5	T4.5	1200/5.5/nc/1.000	1100/4.5/4/1.000	1100/4.5/2/1.000	1100/4.5/nc/0.469	1200/5.5/4/0.982	1100/5.0/4/1.000
			1000/4.5/3/0.366

NOTE. — Only models with $f_{\text{MC}} > 0.1$ are listed.

^a Spectral types of the L dwarfs are from Kirkpatrick et al. (1999), Reid et al. (2000), Gizis et al. (2000), Kirkpatrick et al. (2000), Burgasser et al. (2006a), and J.D. Kirkpatrick (in preparation). Spectral types of the T dwarfs are from Burgasser et al. (2003a, 2006a). Errors on spectral types are ± 0.5 subclass unless otherwise noted.